

We are IntechOpen, the world's leading publisher of Open Access books Built by scientists, for scientists

6,300

Open access books available

171,000

International authors and editors

190M

Downloads

Our authors are among the

154

Countries delivered to

TOP 1%

most cited scientists

12.2%

Contributors from top 500 universities



WEB OF SCIENCE™

Selection of our books indexed in the Book Citation Index
in Web of Science™ Core Collection (BKCI)

Interested in publishing with us?
Contact book.department@intechopen.com

Numbers displayed above are based on latest data collected.
For more information visit www.intechopen.com



Bragg Grating Tuning Techniques for Interferometry Applications

Rogério Dionísio

Abstract

Fiber Bragg grating is widely used in optical fiber applications as a filter or a sensor due to its compact size and high sensitivity to physical conditions, such as temperature and strain. The purpose of this chapter is to describe the implementation and characterization of two tuning methods for optical fiber Bragg gratings, varying the temperature or the length of the fiber. Among the methods using mechanical deformation, compression of the fiber by bending a flexible sheet aggregated with the Bragg grating has shown very interesting tuning results, reaching 19.0 nm with minimum reflection bandwidth variation over the entire tuning range. Stretching the fiber has presented several drawbacks, including breaking of the fiber and a lower tuning range of 4.9 nm. Temperature tuning technique presents good linearity between tuning range and temperature variation but at the cost of a low tuning range (0.4 nm) and a permanent high current electrical source.

Keywords: fiber Bragg grating, tuning system, thermal tuning, mechanical tuning, experimental characterization

1. Introduction

Fiber optic Bragg gratings (FBGs) were first produced in 1978 by Ken Hill et al., during an experiment where an optical fiber was exposed to intense radiation from an argon laser. The interference process started between the incident wave and the 4% light reflected at the opposite end of the fiber [1]. It was not until a decade later, in 1989, that G. Meltz and his team proposed Bragg gratings production process by exposing the fiber transversely to two coherent beams of ultraviolet light, forming an interference pattern in the fiber core [2, 3].

Over the last decades, Bragg gratings have been used as sensors [4, 5] or as optical filters in wavelength division multiplexing (WDM) communication systems [6]. They have found application in devices with routing capacity in the optical domain, as is the case of optical add drop multiplexers (OADM) and optical cross connect (OXC) nodes. They are also used in frequency stabilizers of semiconductor lasers [7], on tunable fiber lasers [8], and in the gain equalization of optical amplifiers [9]. Fiber dispersion compensation [10] is another realization with tunable fiber Bragg gratings.

The evolution of transmission systems from point-to-point connections to dynamically configurable networks brought the need for tunable optical filters. Furthermore,

the increasing transfer of information over fiber optic networks causes an increase in the number of optical channels in Dense (DWDM) or even in Coarse WDM (CWDM). The expansion in the bandwidth necessity range can cover the S, C, L, and U bands, corresponding approximately to 215 nm.

During the last 3 decades, but also very recently, the use of spread spectrum techniques in the optical domain, such as optical code division multiplexing (OCDMA), has stirred the interest of the scientific community, as an option in reconfigurable optical networks [11]. This process allows the various channels to share the same spectral band; each one being identified by a specific code. Other features of this technique should be highlighted: Greater safety in the data transmission, more flexible use of available bandwidth, reducing crosstalk between adjacent channels, and enabling asynchronous communication [12]. The recent use of spectral amplitude coding OCDMA (SAC-OCDMA) in optical coding and decoding systems has brought the ability to eliminate multiple access interference (MAI) [13]. For this technique to be attractive from the point of view of implementation in an optical network, the definition of the codes will have to be flexible [14], so that tunable FBGs are a key element of the process. One of the features that make FBGs attractive is that the reflection spectrum can be tuned from a few nanometers, heating the Bragg grating or applying mechanical tension to the ends (compression or extension).

The objective of this chapter is to describe the implementation of two tuning methods for fiber Bragg gratings, as a function of variations in temperature or in the length of the FBG. Among the methods of mechanical deformation, the deformation of the grating by stretching or compressing the fiber and the deformation by curvature of a flexible blade connected to the Bragg grating are experimentally implemented and discussed.

The rest of the chapter is structured as follows: Section 2 presents the operating principle of FBG tuning techniques using mechanical and temperature techniques. Section 3 describes the experimental measurement setup for FBG tuning characterization. Section 4 presents the main experimental results and discusses the potential of each tuning technique. Finally, Section 5 gives concluding remarks.

2. Operating principle

The resonant wavelength (λ_B) of a Bragg grating depends on the effective refractive index at the fiber core (n_{eff}) and the period of the interference pattern (Λ) [15],

$$\lambda_B = 2 \cdot n_{eff} \cdot \Lambda \quad (1)$$

In turn, these parameters are affected by temperature variations or mechanical deformations. From **Eq. (1)**, the deviation of the Bragg wavelength due to mechanical deformations Δl , or temperature variations ΔT [16] are:

$$\Delta \lambda_B = 2 \left(\Lambda \frac{\delta n_{eff}}{\delta l} + n_{eff} \frac{\delta \Lambda}{\delta l} \right) \Delta l + 2 \left(\Lambda \frac{\delta n_{eff}}{\delta T} + n_{eff} \frac{\delta \Lambda}{\delta T} \right) \Delta T \quad (2)$$

The first term of **Eq. (2)** represents the dependence of λ_B as a function of Δl , caused by variations in the grating period and the change in the effective refractive index. This term can be described by:

$$\Delta\lambda_B = (1 - \rho_e) \cdot \varepsilon_{rel} \cdot \lambda_B, \quad (3)$$

where ε_{rel} is the relative elongation and ρ_e is the effective elasto-optic coefficient. For a silica optical fiber, $\rho_e \approx 0.22$ [17].

The second term of expression (2) represents the effect of temperature on changing the Bragg wavelength. For a Bragg grating with maximum reflectivity at 1550 nm, the typical values of sensitivity to temperature and mechanical stress are, respectively, 13.25 pm/°C and 1.2 pm/με [16].

It is therefore predictable that any change in wavelength associated with external disturbances is the result of the sum of the effects of temperature and mechanical deformations. Therefore, the individual discrimination in the spectral response of the FBG for each source of disturbance needs a method of separating the measurements. Briefly, the existing methods are extrinsic or intrinsic and are reported in detail in [16]. In Section 4.1, a set of tuning experiments is described, based on stretching or compressing the fiber, and which take place in a laboratory in a controlled temperature environment. Under these conditions, the influence of temperature on the wavelength variation is very small compared to the variations induced by the mechanical compression or stretching methods.

2.1 Mechanical linear tuning

Figure 1 illustrates the elements that make up a tuning system by mechanical tension on the fiber. The ends of the optical fiber are fixed on two supports, where at least one must be able to move along the axial axis of the fiber.

The relative elongation along the axial axis is defined by

$$\varepsilon_{rel} = \frac{\Delta z}{L}, L \neq 0, \quad (4)$$

where Δz is the displacement and L is the length of the fiber under the effect of a mechanical deformation [18]. Substituting this result into Eq. (3), we get:

$$\Delta\lambda_B = (1 - \rho_e) \cdot \frac{\Delta z}{L} \cdot \lambda_B, L \neq 0 \quad (5)$$

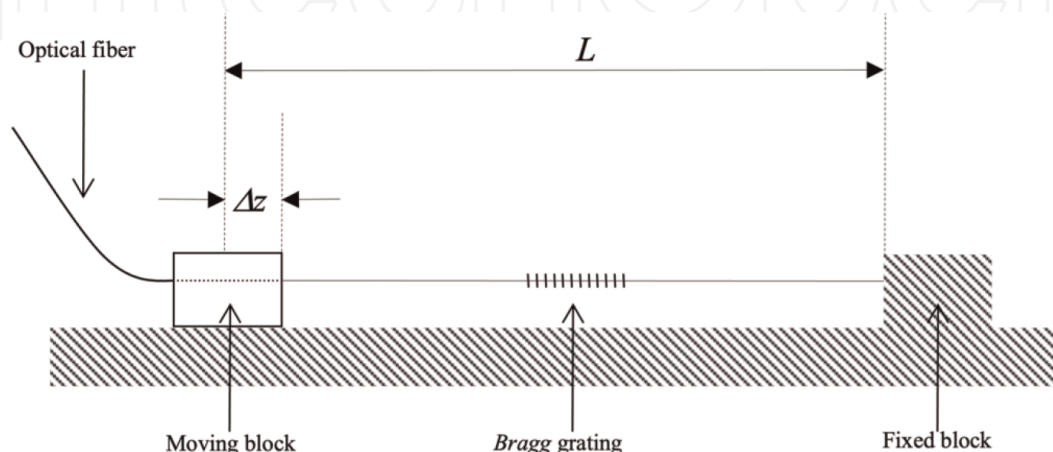


Figure 1.
 Schematic of the structure of a tuning system for fiber optic Bragg networks.

The result is an equation that relates the variation of the Bragg wavelength as a function of the normalized fiber length. The change in wavelength will be positive or negative if the Bragg grating undergoes stretching or compression, respectively. Considering that the displacement is much smaller than the length of the grating, **Eq. (5)** is approximately linear.

2.2 Mechanical tuning by bending

Figure 2 shows the scheme of a tuning system, in which a force is applied to a flexible blade. Horizontal displacement Δz causes the blade to bend in an arc with angle θ . The relationship between the angle arc θ and the displacement Δz is given by:

$$\Delta z = L \left[1 - \frac{\sin\left(\frac{\theta}{2}\right)}{\left(\frac{\theta}{2}\right)} \right], \quad (6)$$

where L is the length of the blade in the initial state, with no force applied to it [19, 20].

For an optical fiber embedded in an elastic material at a distance d from the blade, the relative elongation is given by [19–21]:

$$\varepsilon_{rel} = \mp \frac{d \cdot \theta}{L}, L \neq 0 \quad (7)$$

The negative sign corresponds to a compressive force when the blade is bent upwards, while a positive sign in the second term of **Eq. (7)** indicates a pulling force on the fiber, bending the blade downwards.

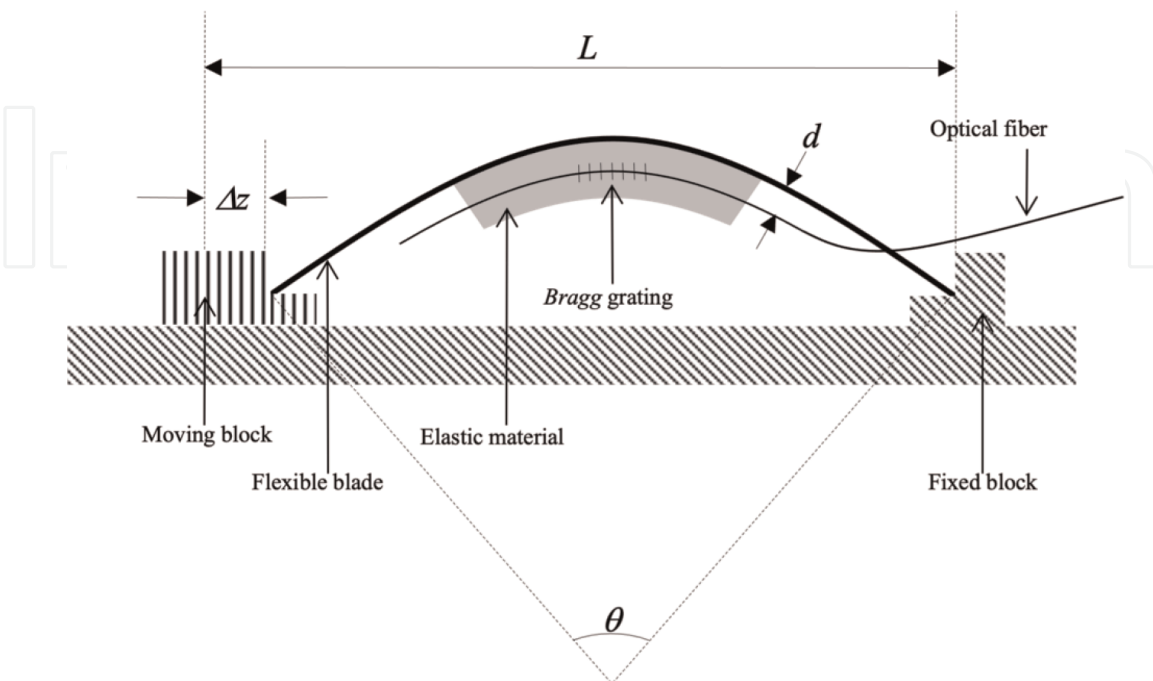


Figure 2. Schematic of the structure of a tuning system based on bending a flexible blade.

Conjugating (3), (6), and (7) into a single equation,

$$\frac{\Delta z}{L} = 1 - \text{sinc}\left(\frac{\Delta\lambda_B \cdot L}{2 \cdot \pi \cdot d \cdot (1 - \rho_e) \cdot \lambda_B}\right), L \neq 0 \quad (8)$$

The relationship between the spectral tuning λ_B and the displacement is not linear, contrary to the result in the procedure in Section 4.1.

2.3 Temperature tuning

The second term of Eq. (2) provides an explicit relationship of the dependence of the Bragg wavelength on temperature variations and is expressed by:

$$\Delta\lambda_B = (\alpha_T + \xi_T) \cdot \Delta T \cdot \lambda_B, \quad (9)$$

where α_T is the thermal expansion coefficient and ξ_T is the thermo-optical coefficient. In the case of silica, the mentioned constants have the following values: $\alpha_T = 0.55 \times 10^{-6} K^{-1}$ and $\xi_T = 8.0 \times 10^{-6} K^{-1}$.

A possible tuning scheme is to place the Bragg grating over a thermoelectric module, also called a Peltier cell, and envelop the set-in thermal mass. The objective is to standardize the temperature in the network and increase the thermal conductivity between the optical fiber and the Peltier module [22, 23].

It is also possible to increase the thermal sensitivity of the optical fiber by fixing it on a metallic surface. If a zinc (Zn) sheet is used, it is possible to increase the sensitivity to 40.8 pm/K. By fixing two Peltier modules at the ends of the zinc sheet, a temperature gradient is created that causes a linear variation of the grating period, which is used to tune the Bragg wavelength, maintaining a constant group delay. For this, the temperature difference between the two ends is kept constant, while the temperature at both ends is increased or decreased by the same amount [24].

3. Laboratory measurement system

To characterize the tuning methods, an optical measurement system was set up, whose implementation scheme is shown in Figure 3. It is based on the measurement of the spectral component reflected by the network when illuminated by an optical

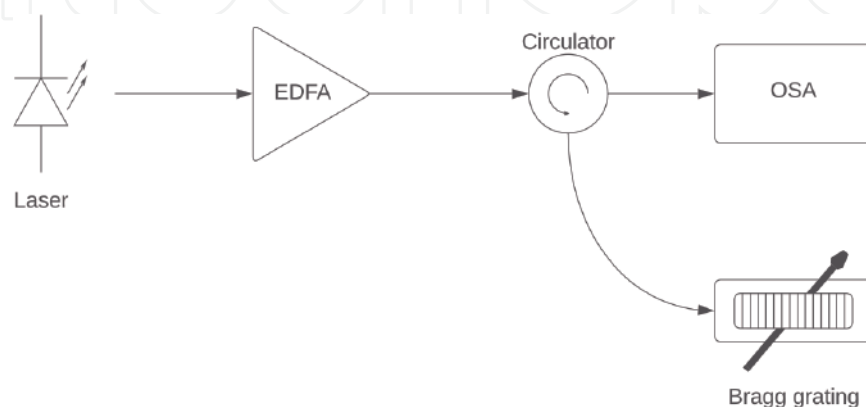


Figure 3.
 Experimental setup used to determine the deviations in the central wavelength of the FBG, caused by the tuning system.

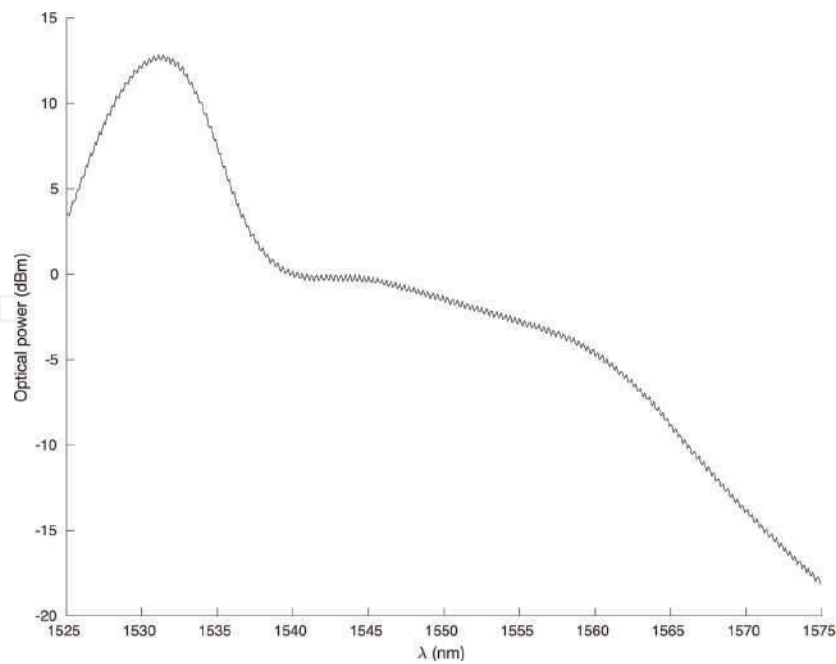


Figure 4.
Optical spectrum of the ASE measured at the amplifier output for an optical pumping power value of 88 mW.

source with high spectral bandwidth. The input optical signal is amplified and introduced into the Bragg grating through an optical circulator. The signal reflected by the FBG is then conveyed by the circulator to an optical spectrum analyzer (ANRITSU model MS9601A). The Bragg grating is tuned by a motorized system developed for this purpose, which is described in ref. [25].

A commercial optical amplifier (Photonetics model BT 13) with a pumping laser at 980 nm and an optical saturation power of 13 dBm was used.

Figure 4 shows the ASE spectrum, measured with a resolution of 0.5 nm, where the dependence of the spectral amplitude with the wavelength is clearly visible. Therefore, all spectral measurements described in the following chapter are represented by subtracting the optical power of the source from the reflection spectrum, at each wavelength.

Bragg gratings are recorded on photosensitive single-mode fiber (Fibercore model PS1250/1500) with numerical aperture 0.13 and diameter 125 μm . The etching method exposes the fiber to ultraviolet radiation through a constant period phase mask. The recording optical source is an Argon laser operating in continuous mode at 244 nm and with an average power of 150 mW. A more detailed description of the recording system can be found in [26, 27]. The apodization format of the network is approximately Gaussian because the laser used has an optical beam with a Gaussian profile.

4. Experimental results and discussion

4.1 Mechanical tuning

The tuning test, based on the scheme in **Figure 1**, is applied to a Bragg network with 1.5 cm long, half-height bandwidth 0.1 nm, center wavelength at 1556.94 nm, and rejection range of 10 dB. The length of the fiber containing the FBG is 18 cm, corresponding to the initial distance between the clamping presses.

According to studies carried out by several authors [18, 19], the maximum relative elongation that can be exerted on a silica optical fiber is 1%. To preserve the elasticity characteristics of the fiber, a more conservative value, around 0.5%, is considered the maximum limit. Regarding the fiber length used, it corresponds approximately to 0.9 mm. In the computerized tuning process, described in [25], this limit is considered to prevent the optical fiber from breaking.

Figure 5 shows the reflection spectrum of the stretched Bragg grating. The maximum deviation from the central wavelength is 4.9 nm and corresponds to an offset of 0.98 mm. According to **Eq. (3)**, the relative elongation was 0.4%, remaining within the preestablished limit.

Figure 6 shows the evolution of the bandwidth at 1, 3, and 10 dB, during the stretching process of the Bragg grating. Specifically, the bandwidth at 1 dB exhibits a variation within the range ± 0.01 nm, for the bandwidth of 3 dB there is an increase of 0.01 nm, and at 10 dB there is an increase of 0.05 nm in the bandwidth. Changes in maximum reflectivity are less than 1.1 dB.

The relationship between the variation of the central wavelength and the relative elongation is shown in **Figure 7**. The deviation from the central wavelength grows linearly as a function of relative elongation, at a rate of 0.85 pm/ $\mu\epsilon$ and with a correlation coefficient of 0.9951. The expected value for the growth rate, using expression (3), would be 1.2 pm/ $\mu\epsilon$.

To verify whether this discrepancy is caused by imperfections in the motorized system, the influence of positioning errors on central wavelength tuning is calculated:

$$|d(\Delta\lambda_B)| \leq \left| \frac{\partial(\Delta\lambda_B)}{\partial(\Delta z)} \right| |d(\Delta z)| = \frac{0.78\lambda_B}{L} |d(\Delta z)|, \tag{10}$$

where $|d(\Delta z)|$ is the tuning system accuracy (15 μm), L is the fiber length (18 cm) and λ_B is the Bragg wavelength of the Bragg grating at rest (1556.94 nm). With these

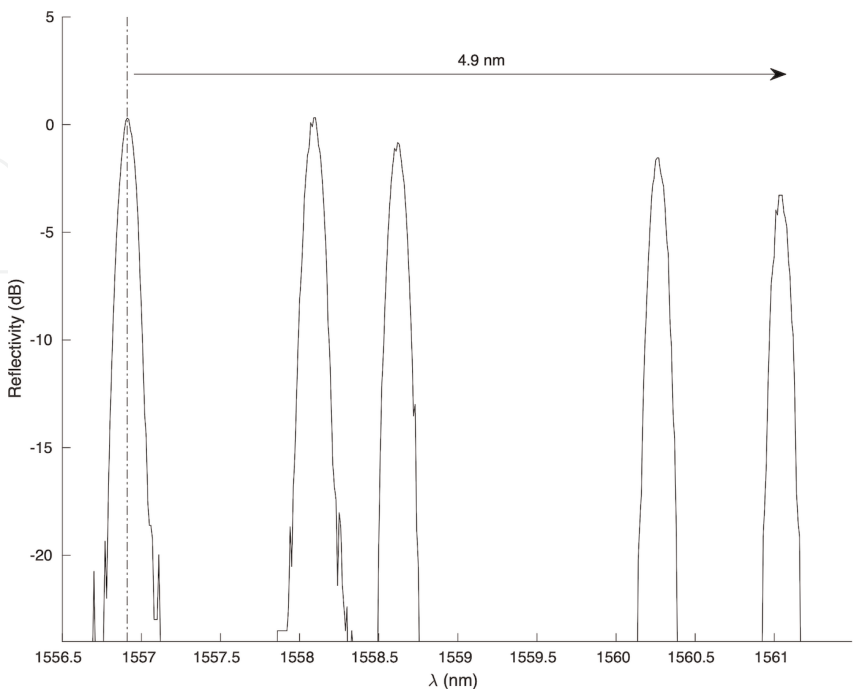


Figure 5.
Reflection profile of a Bragg grating under the effect of mechanical strain.

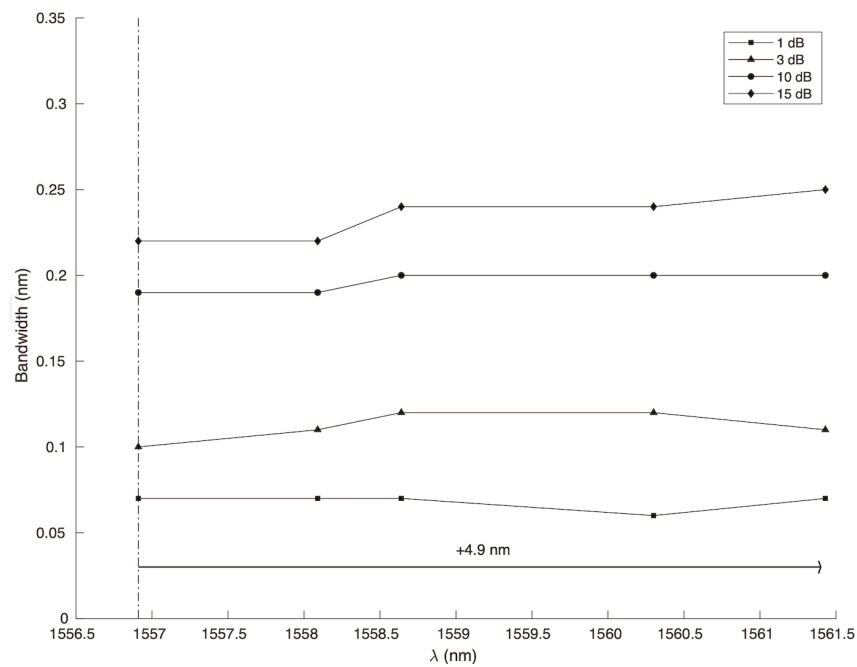


Figure 6.
Bandwidth evolution over the entire tuning range.

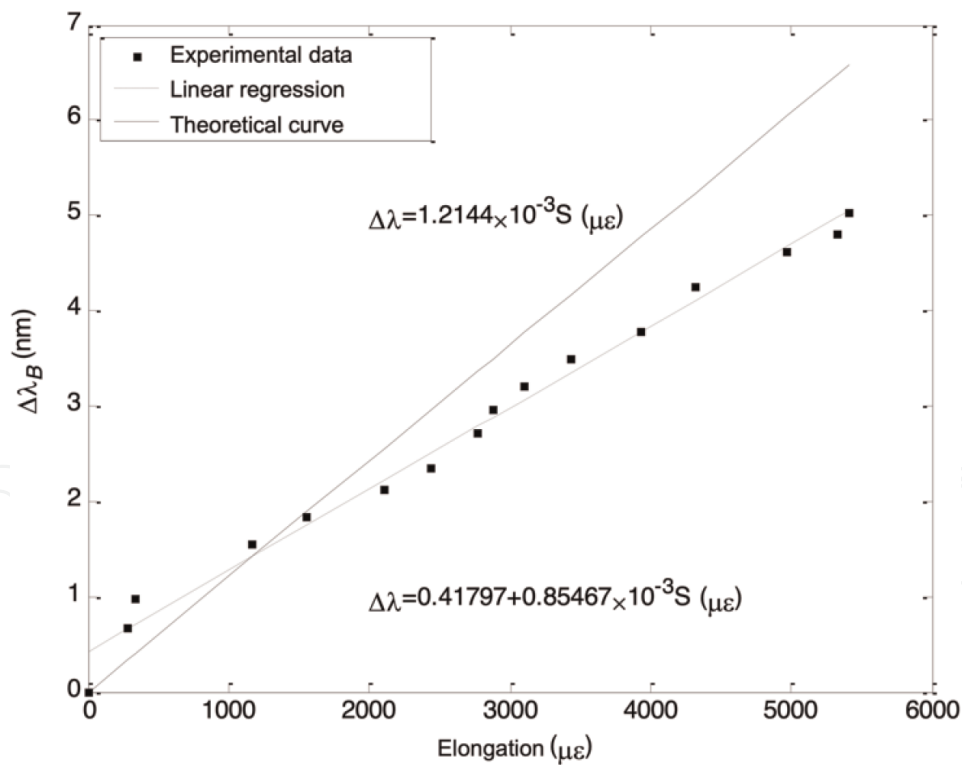


Figure 7.
Bragg wavelength variation as a function of relative elongation.

values, the variation of the tuning value $|d(\Delta\lambda_B)|$ is always less than or equal to 101 pm. If the error $|d(\Delta\lambda_B)|$ is included in the set of measurements performed for the central wavelength, the resulting growth rate is in the range $[0.84228, 0.85467]$ pm/ $\mu\epsilon$. Therefore, imperfections in the motorized system are not the main cause of the differences.

A second tuning test had the scheme described in Section 2.2 as its working principle. In the first stage, the fiber is not embedded in an elastic material but fixed directly to the surface of a flexible sheet. The blade used is 15.2 cm long, 2 cm wide, and 1.5 mm thick, and is made of acrylic. A “v” shaped groove is created along the blade, 9 mm deep, to accommodate the fiber, so that it does not suffer transverse deviations. Consequently, $d = 6$ mm (see Eq. (7)). The assembly is then glued to increase its strength and to properly fix the FBG inside the groove. Finally, the support is placed between the moving and fixed blocks of the tuning system to start the tests.

It was said earlier that the fiber can be stretched up to 1% without suffering irreversible damage. In compression mode, this value can reach 23% [19], which allows much larger tuning ranges than in elongation. Substituting Eq. (7) in (6), the resulting equation allows calculating a priori the maximum displacement allowed without damaging the fiber. Using more conservative values of 0.5% for compression and 11% for relative elongation, the calculated limits are, respectively, 9.96 mm and 14.13 cm.

The Bragg grating used is 2 cm long, it has a 3 dB bandwidth equal to 0.48 nm and a central wavelength of 1550.4 nm. During the tests, the amplitude of the reflection spectrum was recorded by an optical spectral analyzer, at several tuning points, as shown in Figure 8.

The results show that the variation achieved in the central wavelength, using compression, and stretching forces reaches practically 19 nm. It is visible in Figure 8 that there is a gap in the initial phase of the stretching tuning process. This failure occurred simply because the spectral measurement process was started with the Bragg grating already under the effect of a sufficiently strong mechanical stress that the central wavelength was shifted from its initial value of 1550.4 nm.

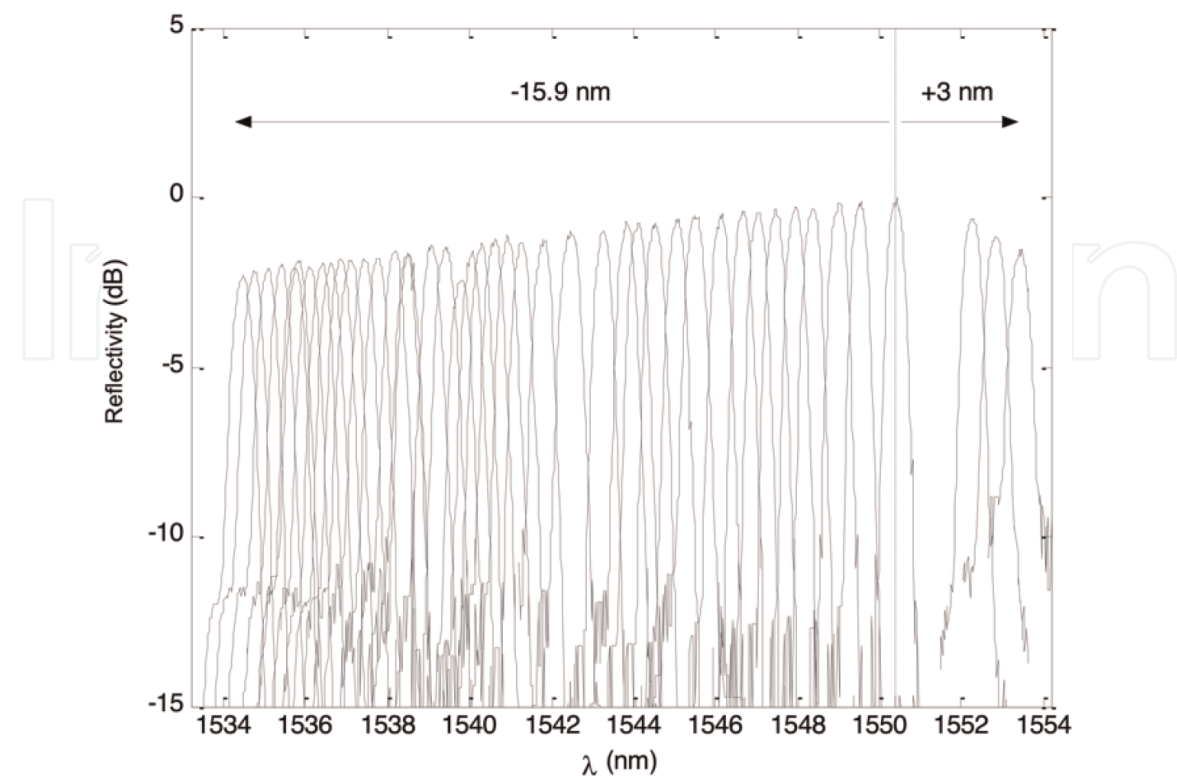


Figure 8.
Tuning the central wavelength of the Bragg grating at 18.9 nm.

It is possible to obtain better results, especially in compression mode, as the mobile platform moved only 6.8 cm to obtain a variation of -15.9 nm. However, the mechanical characteristics of the acrylic sheet did not allow to compress the fiber further. On the other hand, the 3 nm spectral variation in stretching mode was achieved by moving the system 4.3 mm and could theoretically reach 4.2 nm with a displacement equal to 9.96 mm.

Figure 9 shows the relationship between tuning range $\Delta\lambda$ and normalized length $\Delta z/L$.

The results show a good agreement between the theoretical curve, calculated by Eq. (8), and most of the measurements performed.

The main differences are located at the ends of the graph, which correspond to situations of greater mechanical stress. They are somehow correlated with the progressive decrease in the maximum reflectivity amplitude, visible in **Figure 8**. These changes can be caused by undetected problems in the tuning system. In particular, the glue used can lose its fixing qualities when subjected to large deformations, resulting in bends on the fiber [18].

The evolution of the bandwidth at 1, 3, and 10 dB is represented in **Figure 10**. Starting from the initial position, the axial mechanical forces applied on the FBG do not cause great changes in the width at 3 dB, which oscillates between -0.1 and 0.04 nm. The bandwidth at 1 dB also remains practically constant, with a maximum deviation of 12.5% from the initial value. However, the bandwidth at 10 dB undergoes a gradual increase that reaches 0.4 nm in compression and 0.56 nm in stretching, in addition to showing an irregular behavior.

The increase in bandwidth at 10 dB is clearly visible in **Figure 11**, where the reflection spectrum is not symmetrical, especially when the FBG is subjected to strong

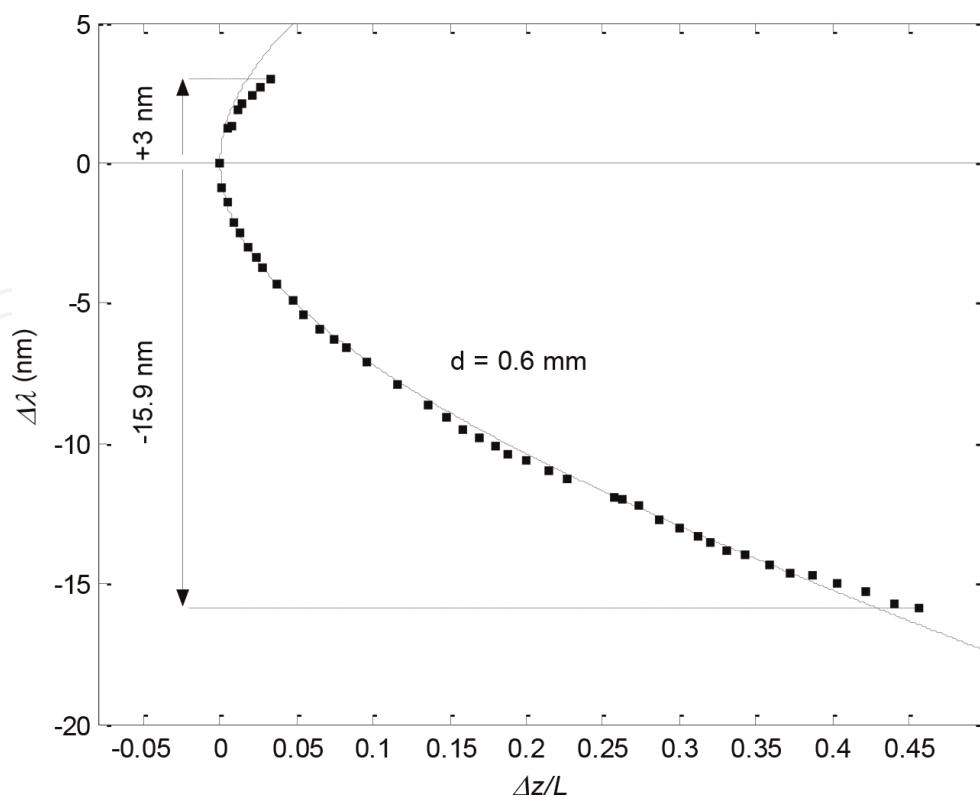


Figure 9. Wavelength variation as a function of normalized horizontal displacement. (Dashed line: theoretical value, points: measured values).

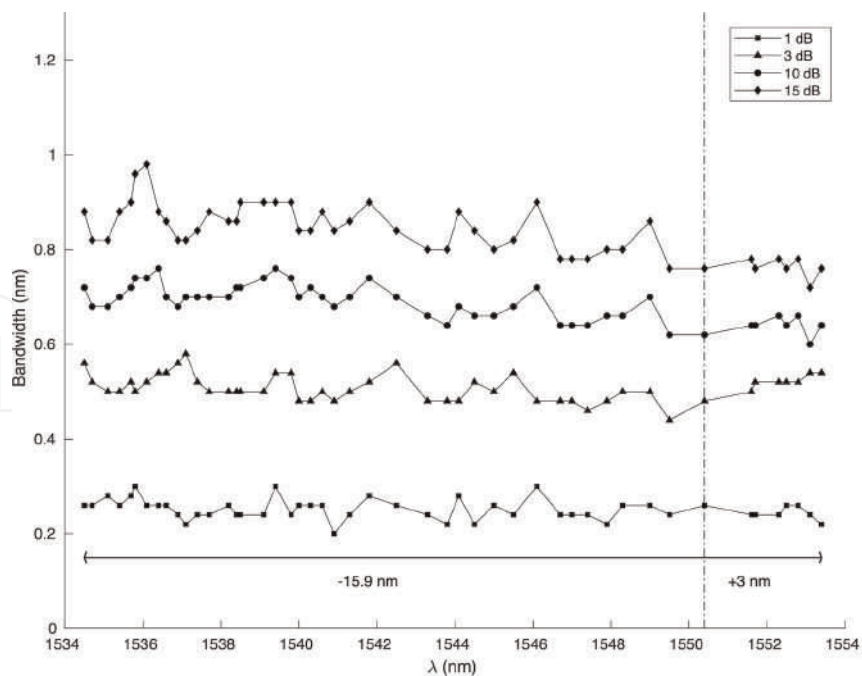


Figure 10.
Bandwidth evolution over the entire tuning range.

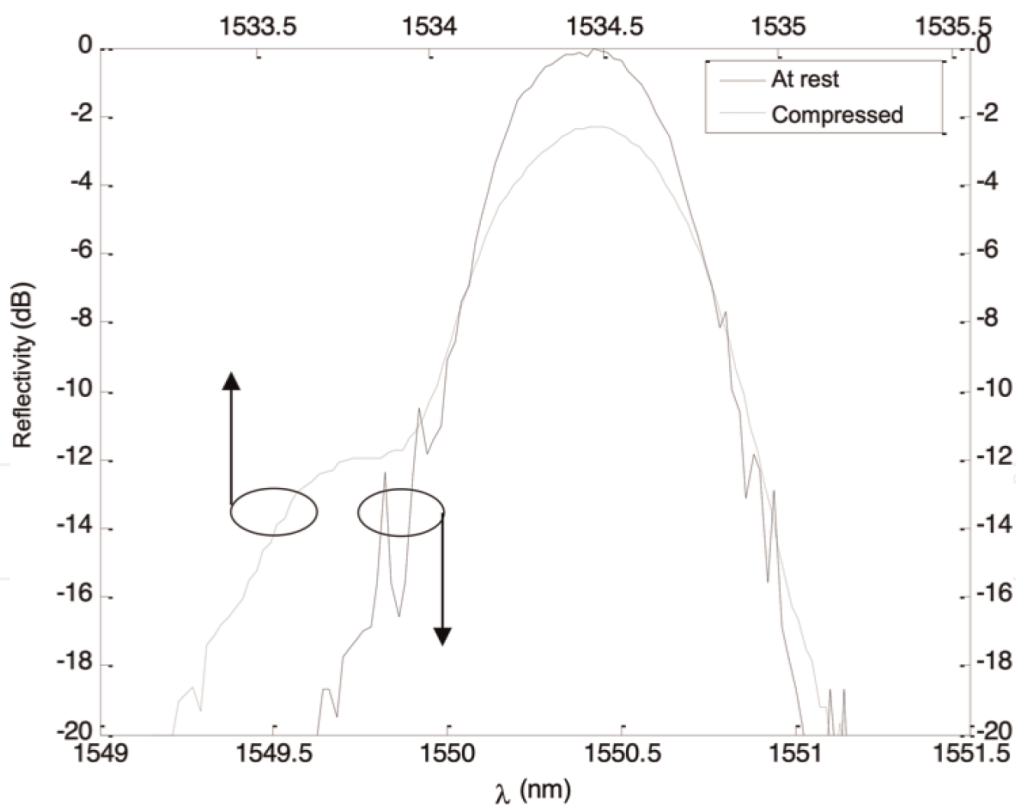


Figure 11.
Spectral response of a Bragg grating at rest (solid line) and under compression (dashed line).

compressions. Under these conditions, the pressure exerted along the grating is not uniform, which causes a variation in the grating period Λ and consequently a chirped spectrum. Consequently, the coupling between the propagation modes within the

FBG is no longer tuned to just one wavelength, thus decreasing the maximum reflectivity amplitude, and increasing the width at the base of the reflection spectrum.

On the other hand, the irregularities observed are largely due to the noise level being very close to 10 dB, causing sudden and profound variations in the reflectivity value.

According to **Eq. (7)**, the tension exerted on a Bragg grating, fixed at a distance d from the flexible blade, makes it possible to increase the tuning range without changing the length L . Theoretically, it is possible to move the reflection spectrum by 50 nm, even for small Δz deviations [7].

Another tuning test was performed with a Bragg grating with a reflectivity peak at 1546.3 nm, 3 dB spectral width equal to 0.46 nm and length 1.5 cm. The FBG was inserted into silicone, 6 mm away from the surface of a flexible acrylic base 16 cm long.

Figure 12 shows the relationship between the tuning range and the normalized travel distance. The measured tuning points do not follow the theoretical curve for $d = 6$ mm. The main cause for this deviation is a cause of the elastic properties of silicone. The curvature of the acrylic base is not followed by the silicone surface where the Bragg grating is inserted. Thus, the resulting tuning is much smaller than expected.

This problem is accompanied by a progressive decrease in the maximum reflectivity amplitude and in the broadening of the reflection spectrum, visible in **Figure 13**. The FBG reflectivity decreases by 3 dB over approximately 8 nm of tuning. The spectral widths at 1, 3, and 10 dB increase by 0.07, 0.29, and 1.33 nm, respectively.

4.2 Temperature tuning

To verify the dependence of the central reflection wavelength of the Bragg grating on temperature, the reflectivity spectrum of a grating centered initially at 1548.11 nm,

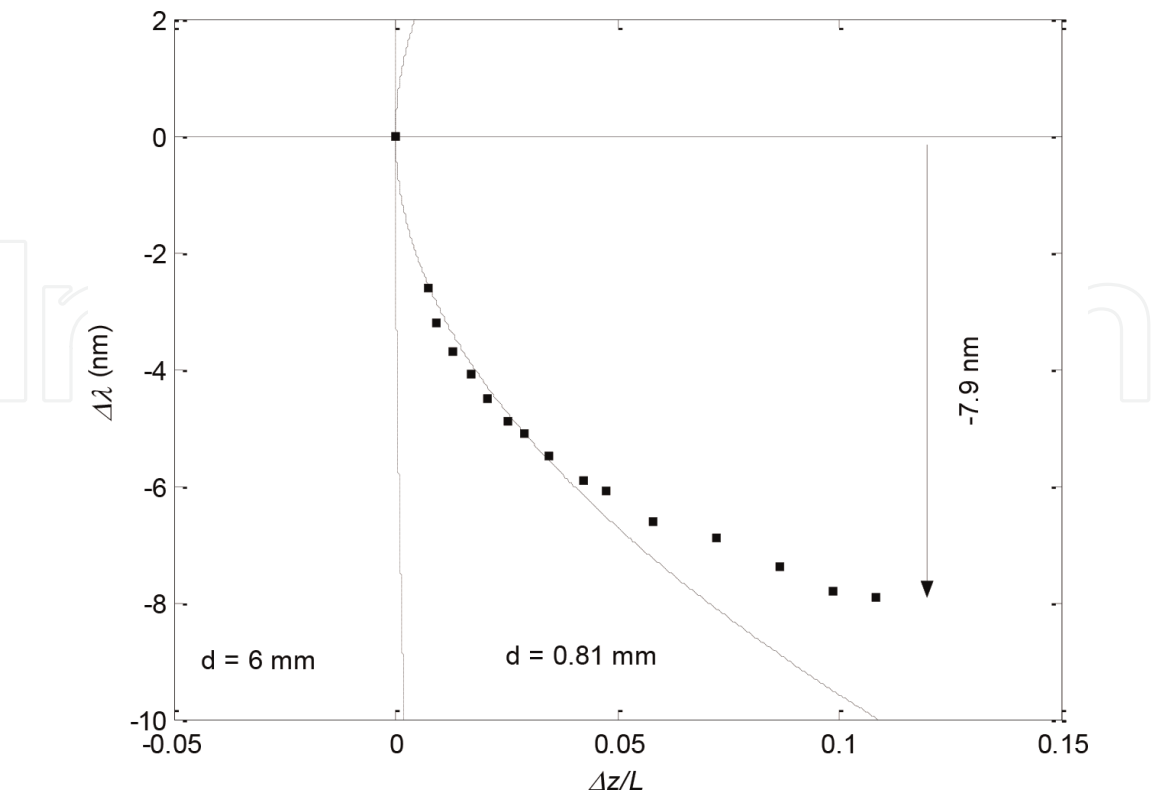


Figure 12. Wavelength variation as a function of normalized horizontal displacement. (Dashed line: theoretical values, points: measured values).

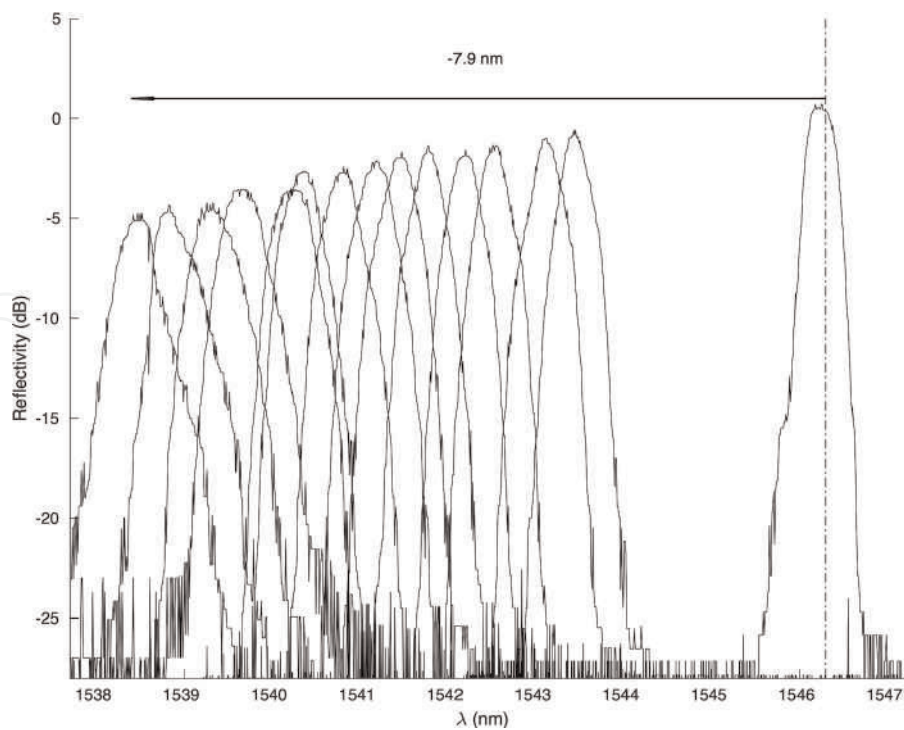


Figure 13.
Bragg grating tuning at 7.9 nm.

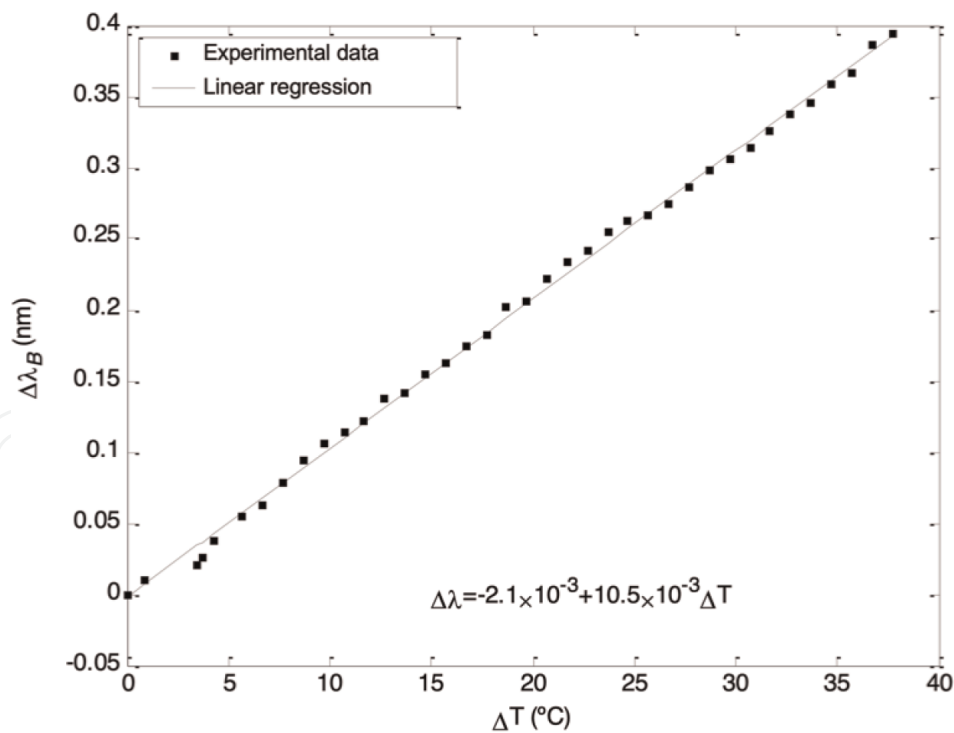


Figure 14.
Bragg wavelength variation as a function of FBG temperature (dashed line: theoretical value, points: measured values).

at a temperature of 14.3°C, was measured. The tuning method is based on the procedure described in Section 2.3. **Figure 14** shows the tuning results achieved at the expense of temperature variation in the Bragg grating. The tuning range accomplished

was 0.4 nm, for a temperature variation of 40°C, and follows a linear relation between temperature and central wavelength variations.

5. Conclusion

In this chapter, two tuning processes for fiber Bragg gratings were presented: By mechanical stress on the fiber grating, or by changing its temperature.

In the first method, the optical fiber is more resistant to compression than to extension. The tuning range of the Bragg grating reflects this behavior, and therefore the Bragg grating must be produced with an initial central wavelength close to the upper tuning limit to increase the effective tuning wavelength span.

In the bending compression method, the material supporting the Bragg grating must be elastic enough to allow it to bend but must have the necessary rigidity to follow the curvature of the acrylic base. Therefore, silicone is not a suitable option for this tuning process, and other material with appropriate properties should be investigated.

The temperature tuning process achieved a poor tuning range (0.4 nm) compared to the mechanical tuning processes (19 nm), and it requires a permanent current source so that the Peltier cells can maintain the fiber grating temperature constant. The mechanical tuning system does not require the use of bulky and expensive current sources and maintains the desired tuning even if the electrical system is turned off. This is an additional advantage, which partially reduces electrical energy consumption. Furthermore, the spectral bandwidth (1, 3, and 10 dB) is maintained over a broad tuning range, but extreme bending or stretching of the fiber may chirp the Bragg grating and increase its spectral bandwidth.


Author details

Rogério Dionísio

Polytechnic Institute of Castelo Branco, DiSAC – Digital Services, Applications and Content, Castelo Branco, Portugal

*Address all correspondence to: rdionisio@ipcb.pt

IntechOpen

© 2022 The Author(s). Licensee IntechOpen. This chapter is distributed under the terms of the Creative Commons Attribution License (<http://creativecommons.org/licenses/by/3.0>), which permits unrestricted use, distribution, and reproduction in any medium, provided the original work is properly cited. 

References

- [1] Hill KO, Fujii Y, Johnson DC, Kawasaki BS. Photosensitivity in optical fiber waveguides: Application to reflection filter fabrication. *Applied Physics Letters*. 1978;**32**(10):647-649
- [2] Meltz G, Morey WW, Glenn WH. Formation of Bragg gratings in optical fibers by a transverse holographic method. *Optics Letters*. 1989;**14**(15):823-825
- [3] Hill KO, Meltz G. Fiber Bragg grating technology fundamentals and overview. *Journal of Lightwave Technology*. 1997;**15**(8):1263-1276
- [4] Russell PS, Archambault JL, Reekie L. Fibre gratings. *Physics World*. 1993;**6**(10):41-46
- [5] Li C, Tang J, Cheng C, Cai L, Yang M. FBG arrays for quasi-distributed sensing: A review. *Photonic Sensors*. 2021;**11**(1): 91-108
- [6] Ahlawat D, Arora P, Kumar S. Performance evaluation of proposed WDM optical link using EDFA and FBG combination. *Journal of Optical Communications*. 2019;**40**(2):101-107
- [7] Giles CR. Lightwave applications of fiber Bragg gratings. *Journal of Lightwave Technology*. 1997;**15**(8):1391-1404
- [8] Radzi NM, Latif AA, Ismail MF, Liew JY, Awang NA, Lee HK, et al. Tunable spacing dual-wavelength Q-switched fiber laser based on tunable FBG device. *Photonics*. 2021;**8**(12):524 MDPI
- [9] Singh H, Sheetal A. Suitability of FBG for gain flatness of 64×10 Gbps DWDM system using hybrid (EDFA + YDFA) optical amplifier in C + L band up to 50 GHz (0.4 nm) channel spacing. *Journal of Optical Communications*. 2019. DOI: 10.1515/joc-2019-0134
- [10] Othonos A, Kalli K, Kohnke GE. Fiber Bragg gratings: Fundamentals and applications in telecommunications and sensing. *Physics Today*. 2000;**53**(5):61
- [11] Hunter DB, Minasian RA. Programmable high-speed optical code recognition using fibre Bragg grating arrays. *Electronics Letters*. 1999;**35**(5): 412
- [12] Cheng HC, Wijanto E, Lien TC, Lai PH, Tseng SP. Multiple access techniques for bipolar optical code division in wireless optical communications. *IEEE Access*. 2020;**8**: 83511-83523
- [13] Boukricha S, Ghoumid K, Mekaoui S, Ar-Reyouchi E, Bourouina H, Yahiaoui R. SAC-OCDMA system performance using narrowband Bragg filter encoders and decoders. *SN Applied Sciences*. 2020;**2**(6):1-9
- [14] McGeehan JE, Hauer MC, Willner AE. Optical header recognition using fiber Bragg grating correlators. *IEEE LEOS Newsletter*. 2002;**16**(4):29-32
- [15] Agrawal GP. *Applications of Nonlinear Fiber Optics*. London Elsevier: Ap, Academic Press; 2021
- [16] Othonos A, Kalli K. *Fiber Bragg gratings: Fundamentals and Applications in Telecommunications and Sensing*. Boston, Mass.: Artech House; 1999
- [17] Ibsen M, Set SY, Goh GS, Kikuchi K. Broadband continuously tunable all-fiber DFB lasers. *IEEE Photonics Technology Letters*. 2002;**14**(1):21-23

- [18] Iocco A, Limberger HG, Salathe RP, Everall LA, Chisholm KE, Williams JAR, et al. Bragg grating fast tunable filter for wavelength division multiplexing. *Journal of Lightwave Technology*. 1999; **17**(7):1217-1221
- [19] Goh CS, Mokhtar MR, Butler SA, Set SY, Kikuchi K, Ibsen M. Wavelength tuning of fiber Bragg gratings over 90 nm using a simple tuning package. *IEEE Photonics Technology Letters*. 2003;**15**(4):557-559
- [20] Mokhtar MR, Goh CS, Butler SA, Set SY, Kikuchi K, Richardson DJ, et al. Fibre Bragg grating compression-tuned over 110 nm. *Electronics Letters*. 2003; **39**(6):509
- [21] Set SY, Dabarsyah B, Goh CS, Katoh K, Takushima Y, Kikuchi K, et al. A widely tunable fiber Bragg grating with a wavelength tunability over 40 nm. In *Optical Fiber Communication Conference 2001 Mar 17* (p. MC4). Optical Society of America
- [22] Mokhtar MR, Ibsen M, Teh PC, Richardson DJ. Simple dynamically reconfigurable OCDMA encoder/decoder based on a uniform fiber Bragg grating. In *Optical Fiber Communication Conference 2002 Mar 17* (p. ThGG54). Optica Publishing Group
- [23] Ohn MM, Alavie AT, Maaskant R, Xu MG, Bilodeau F, Hill KO. Dispersion variable fibre Bragg grating using a piezoelectric stack. *Electronics Letters*. 1996;**32**(21):2000
- [24] Dabarsyah B, Goh CS, Khijwania SK, Set SY, Katoh K, Kikuchi K. Adjustable dispersion-compensation devices with wavelength tunability based on enhanced thermal chirping of fiber Bragg gratings. *IEEE Photonics Technology Letters*. 2003;**15**(3): 416-418
- [25] Dionísio RP. Módulo de Posicionamento Micrométrico: Projecto, Construção e Caracterização. 1º Workshop de Investigação e Desenvolvimento em Engenharia Eletrotécnica e das Telecomunicações [Internet]. 2004 Feb 18 [cited 2022 Jun 27]. pp. 43-48. Available from: <http://hdl.handle.net/10400.11/8003>
- [26] de Brito André PS. Componentes optoelectrónicos para redes fotónicas de alto débito (Doctoral dissertation, Universidade de Aveiro (Portugal))
- [27] Nogueira RN. Redes de Bragg em fibra óptica (Doctoral dissertation, Universidade de Aveiro (Portugal))

We are IntechOpen, the world's leading publisher of Open Access books Built by scientists, for scientists

6,300

Open access books available

171,000

International authors and editors

190M

Downloads

Our authors are among the

154

Countries delivered to

TOP 1%

most cited scientists

12.2%

Contributors from top 500 universities



WEB OF SCIENCE™

Selection of our books indexed in the Book Citation Index
in Web of Science™ Core Collection (BKCI)

Interested in publishing with us?
Contact book.department@intechopen.com

Numbers displayed above are based on latest data collected.
For more information visit www.intechopen.com



Chapter

A Review of Optical Interferometry Techniques for Quantitative Determination of Optically Active Materials in a Solution

*Rahim Ullah, Raja Yasir Mehmood Khan
and Muhammad Faisal*

Abstract

Human diet is primarily comprised of optically active ingredients like glucose, sucrose, fructose, amino acids, lactic acid, cholesterol etc. Quality control is one of the most important processes in food industries to test, measure and verify the product for quality control standards. Optical techniques are mostly adopted in these industries for standardization of purity and concentration of optically active ingredients in their products. Quantitative measurements of optically active materials (OAMs) in a solution by interferometry have attracted the attention in present days due to their wide working range, high sensitivity and lower limit of detection. OAMs cause rotation of the angle of polarization when a plane-polarized light passes through them. The angle of rotation is distinct for different materials at different concentrations. For interferometric quantitative determination, the OAMs are generically placed in an arm of the interferometer and their effect on the interference fringe patterns are monitored as a function of their concentrations. Furthermore, the refractive indices of OAMs varies with their concentrations which directly affect the resultant interference pattern. Owing to the vast range of interferometric arrangements and processing techniques, this review assesses the different approaches adopted in detection of concentration of OAMs in a solution by interferometry.

Keywords: optically active materials, interferometry, refractive index, limit of detection, sensitivity

1. Introduction

Optically active materials are the fundamental constituents of the human body and its nutrients. Major part of the daily human diet is comprised of OAMs, and has a strong impact upon wellness and performance of the human body. The monitoring of OAMs in everyday nutrition is of vital importance for being healthy, lean and active. Therefore, a strong check of quality control is always the matter of concern is the

industries including food, chemical, pharmaceutical, beverages etc. The OAMs cause the rotation in the angle of polarization of linearly polarized light when it pass through them. The variation in plane of polarization is different for different materials at different concentrations. OAMs are not limited to sugar (glucose, sucrose, fructose, maltose etc.), proteins, acids (tartaric acid, lactic acid etc.), cholesterol, etc.

A number of prescribed analytical techniques have been employed such as Ultra-violet visible (UV-vis) absorption spectroscopy [1, 2], thin-layer chromatography (TLC) [3], infrared (IR) and Fourier transform infrared (FTIR) spectroscopy [4, 5] and Raman spectroscopy [6, 7]. However, optical techniques such as polarimetry [8, 9], interferometry [10, 11] and refractrometry [12] are commonly used in most of the practical applications for quantitative determination of OAMs due to their rapidity, noninvasiveness and non-destructive nature of their method of analysis.

OAMs are usually comprised of at least one asymmetric atom inside their molecular structure. The list of those atoms include carbon, sulfur, phosphorous, silicon etc. The asymmetric nature of these molecules result in the formation of two different types of isomers. The isomer of the same substance which rotates the plane of polarization of the light clockwise is called dextrorotatory or right-handed. However, those molecules which cause anti clock wise rotation of the polarization is called levorotatory or left-handed. Optical activity is the result of left-right asymmetry around the central carbon atom in the case of amorphous substances. The geometrical shape and chemical composition of both the molecules are same but left-handed isomer is mirror image of right-handed isomer and both of them are called enantiomers, as shown **Figure 1** for the D and L configuration of glucose molecule. Both of the enantiomorphs rotate the plane of polarization of light exactly by same magnitude but in opposite directions.

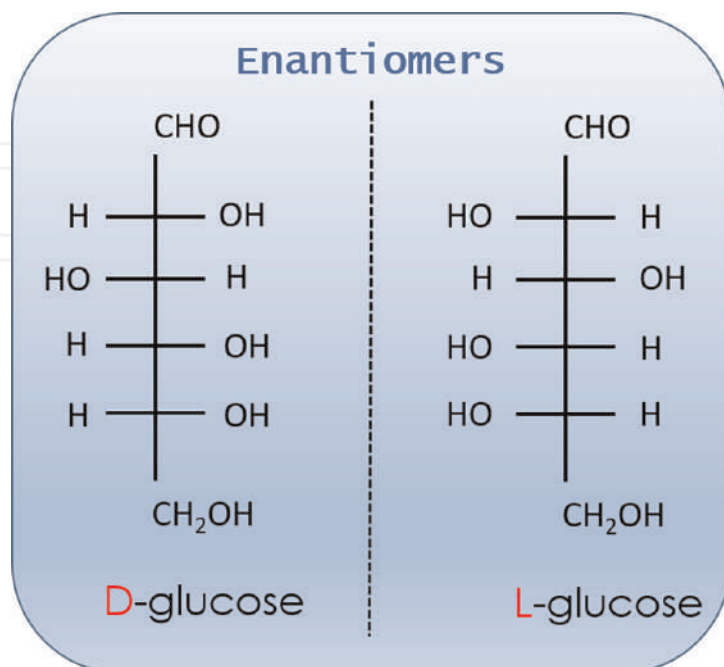


Figure 1.
Dextrorotatory and levorotatory configuration of glucose molecule.

2. Theoretical analysis

2.1 Biot's law

The foundation of detection of analytes concentration by using optical polarimetry trace back to the observation of Biot's in early nineteenth century [13]. The mathematical equation for the optical interaction of linearly polarized light with optically active specimen was described as below which is also called Biot's law;

$$[\alpha]_{\lambda}^T = \frac{\alpha}{LC} \quad (1)$$

The term $[\alpha]_{\lambda}^T$ is known as specific rotation of the OAM under consideration for specific wavelength of light (λ) at temperature (T). Where, α is the detected rotation of plane of polarization of light, L is the path length of the sample under test and C is the concentration of sample.

2.2 Analytical treatment of interference of linearly polarized light beams

Suppose two monochromatic light beams with same frequency originating from single source represented by the electric field vector \vec{E}_1 and \vec{E}_2 and interfere at the point of observation P. Let the light beams are generalized by the equations below however, physical waves will be represented by their real parts only

$$\vec{E}_1 = \vec{E}_{01}e^{-i(\omega t - k_1 \cdot r - \phi_1)} \quad (2)$$

$$\vec{E}_2 = \vec{E}_{02}e^{-i(\omega t - k_2 \cdot r - \phi_2)} \quad (3)$$

Where ω is the angular frequency of the monochromatic light wave, r is the position vector of incident point P, k_1 and k_2 are the wave vectors and ϕ_1 and ϕ_2 are the phase differences of beam 1 and 2, respectively. According to the principle of superposition, the irradiance at point 'P' can be calculated as:

$$I_P = \vec{E}_1 + \vec{E}_2 \quad (4)$$

The time averaged irradiance is proportional to the square of the amplitude of the electric field, i.e., for linear, homogeneous, isotropic dielectric medium;

$$I = \epsilon v \langle E^2 \rangle_T \quad (5)$$

Where ϵ is the permittivity of the medium and v is the velocity of light in that medium. Considering the relative irradiance within the same medium except for the constant of proportionality, Eq. (4) may be transformed into;

$$I_P = \vec{E}_P \cdot \vec{E}_P^* = (\vec{E}_1 + \vec{E}_2) \cdot (\vec{E}_1 + \vec{E}_2)^* = I_1 + I_2 + I_{12} \quad (6)$$

Where,

$$I_1 = \vec{E}_1 \cdot \vec{E}_1^* = E_{01}^2 \quad (7)$$

$$I_2 = \vec{E}_2 \cdot \vec{E}_2^* = E_{02}^2 \quad (8)$$

and

$$I_{12} = \vec{E}_1 \cdot \vec{E}_2^* + \vec{E}_2 \cdot \vec{E}_1^* = \vec{E}_{01} \cdot \vec{E}_{02} (e^{i\delta} + e^{-i\delta}) = 2\vec{E}_{01} \cdot \vec{E}_{02} \cos \delta \quad (9)$$

Where,

$$\delta = (\vec{k}_1 - \vec{k}_2) \cdot \vec{r} + (\phi_1 - \phi_2) \quad (10)$$

The I_1 and I_2 are the irradiance of the individual beams and I_{12} represents the interference term. The symbol, δ represents the total phase difference between the two waves at the point of interest P. From Eq. (9) it can be observed that maximum inference will occur if both the beams are parallel to each other and no interference will occur if both the vectors are orthogonal to each other. For maximum interference Eq. (9) can be written as;

$$I_{12} = 2E_{01}E_{02} \cos \delta = 2\sqrt{I_1 I_2} \cos \delta \quad (11)$$

and total irradiance at point P will become

$$I_P = I_1 + I_2 + 2\sqrt{I_1 I_2} \cos \delta \quad (12)$$

The interference is called fully constructive if $\cos \delta = 2n\pi$ where $n = 0, 1, 2, \dots$ then Eq. (12) can be written as;

$$I_P = I_1 + I_2 + 2\sqrt{I_1 I_2} \quad (13)$$

Eq. (13) is called the maximum intensity or the maxima of fringes pattern (constructive interference) and can be interpreted as;

$$I_{\max} = (E_{01} + E_{02})^2 \quad (14)$$

and I_P will be minimum if the term $2\sqrt{I_1 I_2} \cos \delta$ is negative, i.e., $\cos \delta = -1$ which is possible only if $\cos \delta = (2n + 1)\pi$ for $n = 0, 1, 2, \dots$, and I_P will be called I_{\min} ;

$$I_{\min} = I_1 + I_2 - 2\sqrt{I_1 I_2} = (E_{01} - E_{02})^2 \quad (15)$$

If the two interfering light waves are mutually coherent then the time averaged value of $\cos \delta$ overtime period T should not vanish and a stationary fringe pattern will be obtained in space i.e.,

$$\langle \cos \delta \rangle_T = \frac{1}{T} \int_0^T \cos \delta \, dt \neq 0 \quad (16)$$

At different points of observation (\vec{r}), different values of $\langle \cos \delta \rangle_T$ will be obtained and resultantly different intensities will be obtained at different locations in space. Also $(\phi_1 - \phi_2)$ should not vary in time otherwise $\langle \cos \delta \rangle = 0$ and no sustained

interference fringe pattern will be obtained. The quality of interference fringes is quantitatively described by visibility (V):

$$V = \frac{I_{\max} - I_{\min}}{I_{\max} + I_{\min}} \quad (17)$$

Where I_{\max} and I_{\min} represents the irradiances corresponding to maximum and adjacent minimum in the interference fringes. If one beam is incident with some small angle θ with respect to the plane of incidence then visibility could be defined as;

$$V = \frac{2\sqrt{I_1 I_2} \cos \psi}{I_1 + I_2} \quad (18)$$

Where, I_1 and I_2 are the irradiances of reference and sample beams respectively and ψ is the polarization angle of the sample beam of the interferometer [14].

3. Interferometry for OAMs detection

3.1 Mach-Zehnder interferometer

The Mach-Zehnder interferometer is most commonly used for sensing applications and was first introduced by Ludwig Zehnder in 1891 and Ludwig Mach in 1892 independently. In this interferometer, a coherent light beam is split into two using beam splitter and then recombined on another beam splitter with the help of two mirrors to obtain interference pattern. One part of the splitted beam is called reference while other one is called sensing arm. The chiral sample is kept in the sensing arm of the interferometer and its effect on the contrast of the interference fringes is detected. The interference fringes are normally recorded by a camera and analyzed by image processing techniques. MZI has good potential for the detection of OAMs therefore, most of the time exercised in the literature for this purpose.

Calixto et al. proposed a Mach-Zehnder interferometer (MZI) based wavefront division polarimeter for the measurements of chiral solute concentrations in solutions as shown in **Figure 2**. An optically active solution was kept in a sample chamber in the sensing arm of a MZI. One beam of the polarized light was passed through a liquid sample containing dissolved OAM while the other half of the light was used as reference beam. The plane of polarization of the incident linearly polarized light was rotated when the sample beam propagated through the chiral solutions. As a result, a decrease in the visibility of the interference pattern was observed with increase in the concentration of the OAMs in the solution. Contrast of the interference fringe pattern was maximum when both the sample and reference beams presented a polarization perpendicular to the plane of incidence. However, the visibility of the fringe pattern was deteriorated fully when the polarization of the sample beam is oriented parallel to the plane of incidence. The effect of decrease in the fringes visibility was mainly due to the increase in the refractive index of the solution with increase in the concentration of the OAMs as shown in **Figure 3**. The following calibration equation was obtained for variation of the visibility of the fringe pattern and concentration of the fructose solution:

$$V(c) = 0.643 - 0.31c^2 + 0.048c^4 \quad (19)$$

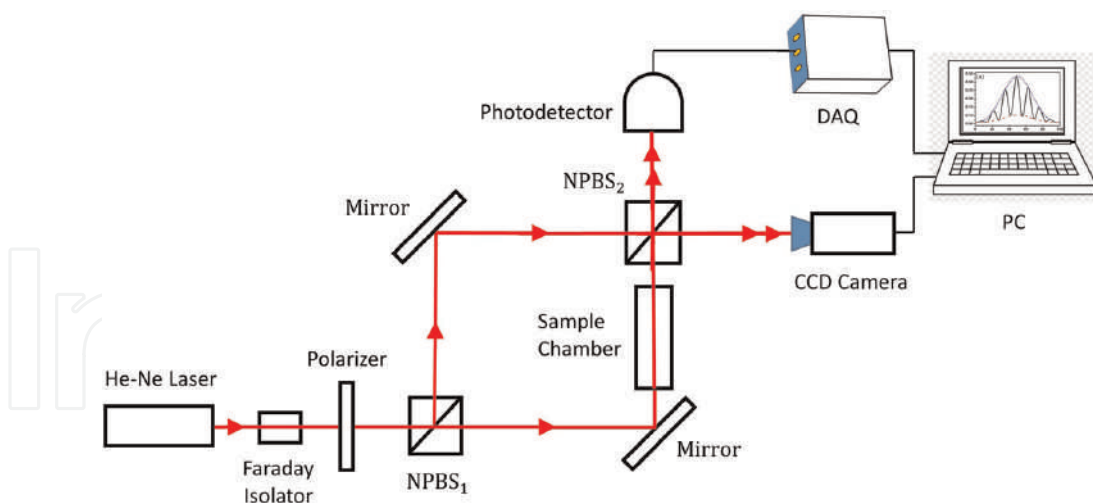


Figure 2. Schematic diagram of the Mach-Zehnder interferometer and interference fringes pattern recording system [14].

Where, ‘V’ is the visibility of the interference fringe pattern and ‘c’ is the concentration of the chiral materials (**Figure 3**).

H.A. Razak et al. proposed an optical sensor based on fiber optic MZI for food composition detection as depicted in **Figure 4**. The MZI structure was employed as fiber optic sensor in single mode-multimode-single mode (SMS) structural configurations using fusion splicing technique. The interferometer was investigated with 4 cm and 8 cm sensing regions. The sensor response was tested for detection of water, sugar and oil from their respective refractive indices as representative major components of food. A red-shift was seen in the wavelength for increase in the refractive index of the constituent sample. The sensitivity of the sensor was found to be directly dependent on the length of the sensing region.

A miniature broad-band (BB) MZI was proposed by M. Kitsara et al. for the detection of label-free biochemical OAMs sensing as shown in **Figure 5**. A theoretical investigation was performed on Si-based MZI with BB input lights in the range 450 nm – 750 nm. They have proved that BB-MZI can be used as a miniaturized optical sensor with enhanced sensitivity, versatile biochemical sensing applications and economical fabrication and operating costs compared to its counterpart single wavelength (SW) MZI. Glucose was used as a representative biomolecular entity because of its relatively small size to demonstrate the designed BB-MZI to detect its concentration in a very diluted solutions with a higher efficiency. The phase changes of the evanescent field at Nd:YAG (532 nm) and He-Ne (633 nm) lasers were studied to evident that an optical setup could be designed where the source of light and MZI chip vary according to application. The theoretical transmission spectra of BB-MZI as a function of the refractive index of the solution were reported for 10 mM, 25 mM, 50 mM and 100 mM glucose concentrations. The recorded peak shifted with concentration of glucose. The performance of the BB-MZI was also observed with a hypothetical protein adlayer over the sensing arm of length 300 μm . An ultra-thin protein adlayer was sensed with recording of the spectral changes or by observing the variation in the integrated intensity. The potential of the designed interferometer was investigated for biomedical applications. It was observed that the performance of the BB-MZI is comparable to the SW-MZI without a requirement of a costly laser system as an input light source.

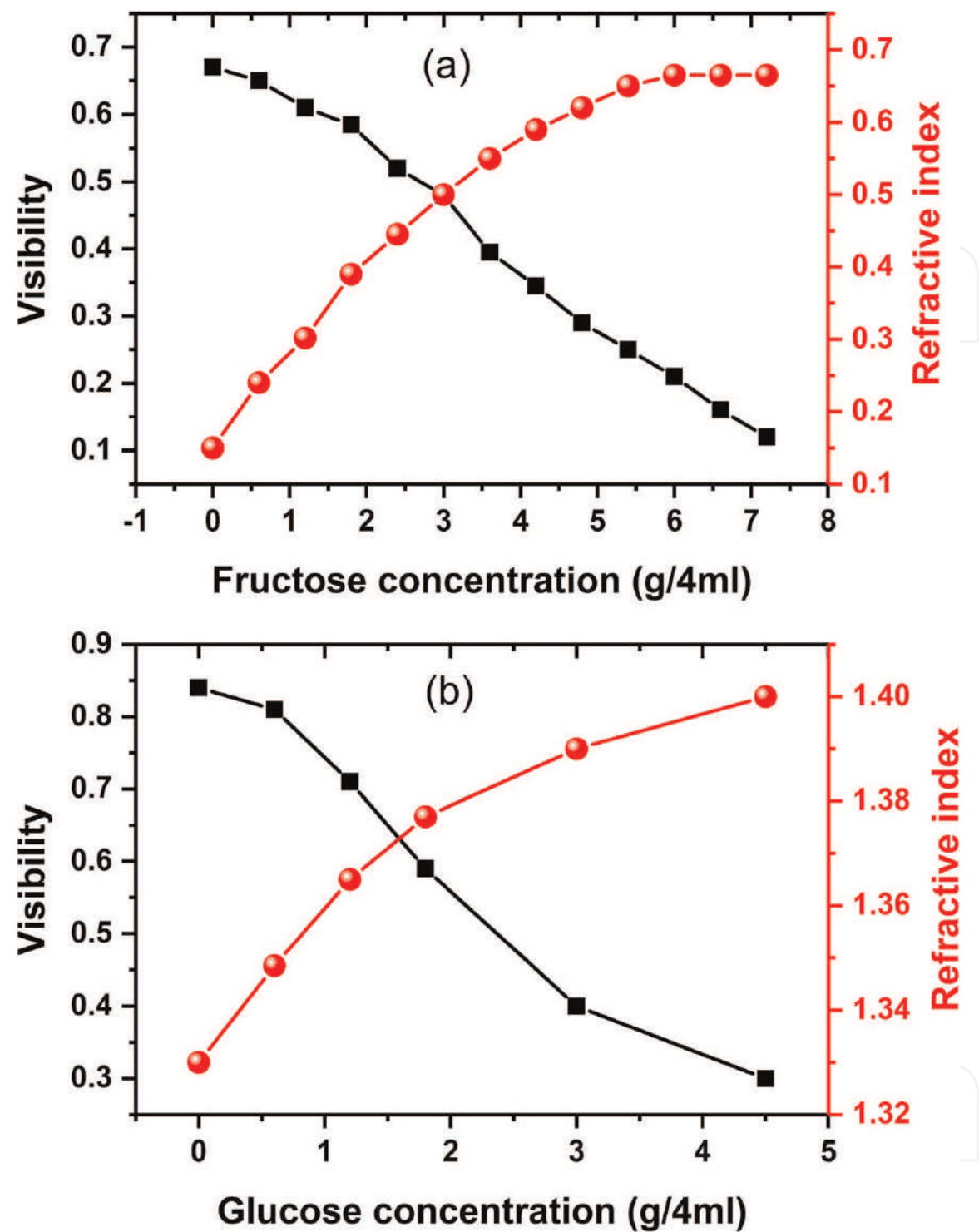


Figure 3.
The effect of concentration on the visibilities of fringes pattern by solutions of (a) fructose and (b) glucose [14].

A. Psarouli et al. also investigated a monolithically integrated BB-MZI for label free detection of biomolecules with high sensitivity as shown in **Figure 6**. A transducer based on monolithic silicon microphotonic was developed for this purpose. The MZI was fabricated from monomodal silicon nitride waveguides with silicone light emitting diodes (LEDs). BB light was injected into the interferometer setup and were sinusoidal modulated by optically active biomolecules with two different frequencies of the polarization before exiting the sensor. The distinct reporting of the two polarizations and simultaneous investigation of the TE and TM signals were performed by

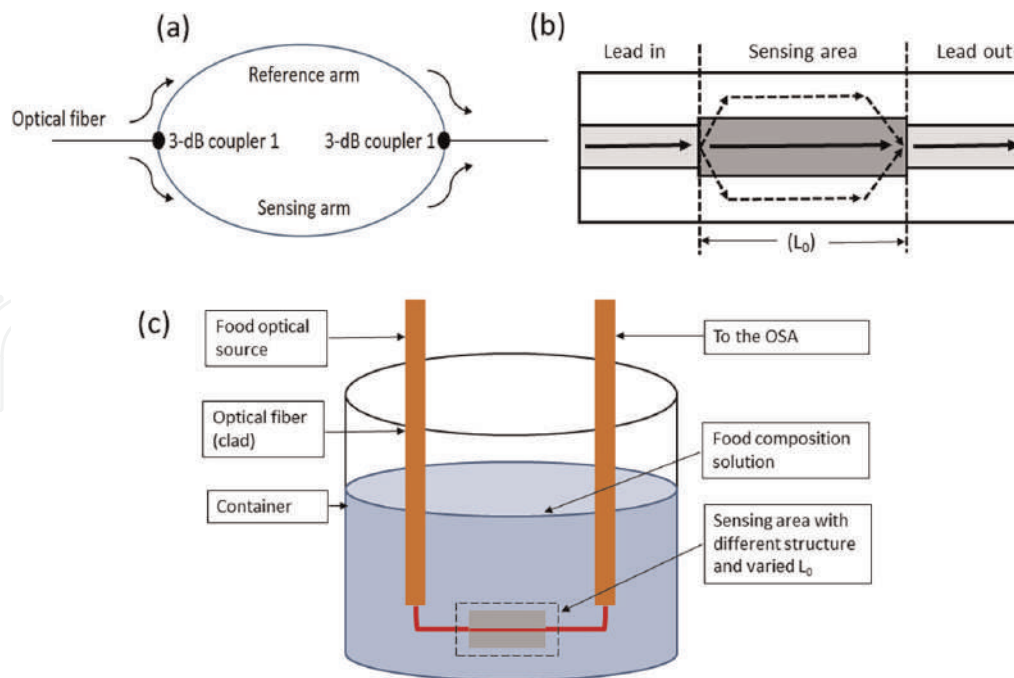


Figure 4. (a) Basic block diagram of optical fiber MZ interferometer. (b) Schematic representation of SMS structure. (c) Schematic diagram of liquid concentration detector [15].

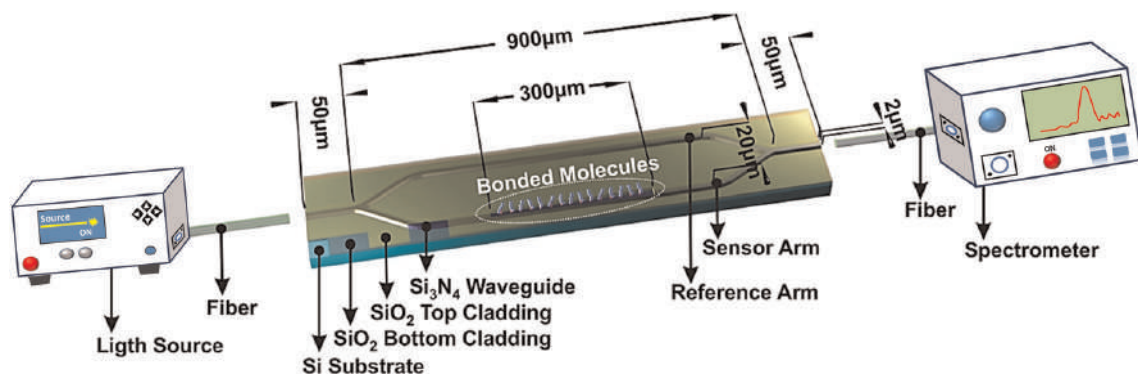


Figure 5. Schematic diagram of the proposed BB-MZI for detection of label-free biochemical chiral materials sensing [16].

deconvolution in the Fourier transform. The quantitative determination of the binding adlyayers were made possible from their refractive indices by dual polarization analysis over the broad spectral range. The sensor was equipped with power and control electronics, a docking station, an off-chip fluidic circuit, a miniature spectrometer and an optical module. The set of ten interferometers were interrogated with a defined time delay by integrated LEDs which were operated by control electronics. The proposed interferometric sensor was found 60 and 550 times more sensitive than a two-lateral-mode spiral waveguide MZI [18] and polyimide-waveguide MZI [19], respectively.

An asymmetric Mach-Zehnder interferometer (aMZI) was introduced by M. J. Goodwin et al. for interferometric biosensing applications [11]. The device was manufactured using TriPleX technology. The interferometer was fabricated on a chip consist of Si₃N₄ waveguide with silica cladding which made a photonic integrated circuit (PIC). A sensing window was fabricated by locally removing the SiO₂ cladding which given a provision to analyte to make a contact with the waveguide. In the

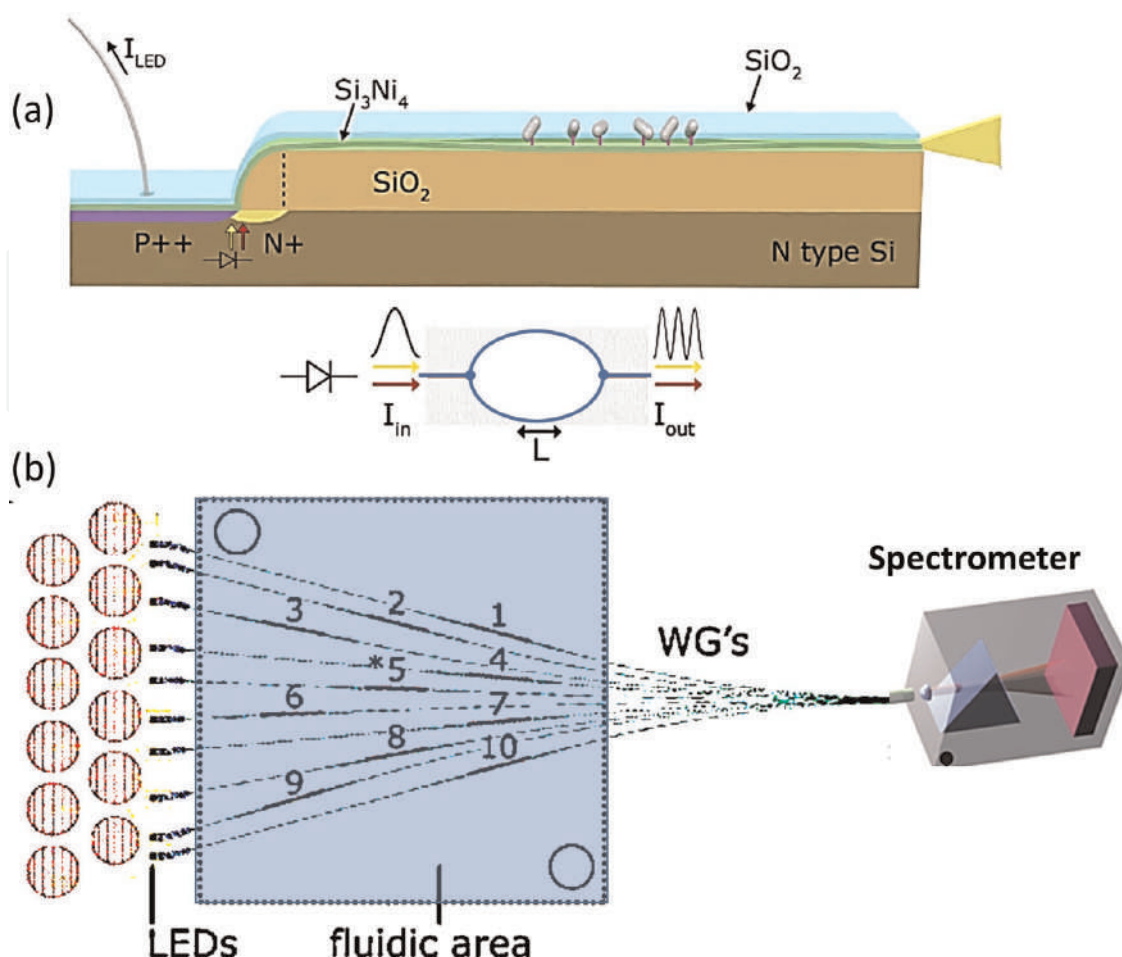


Figure 6.
 (a) Schematic of the biochip showing the monolithic integration of the avalanche-type LED, the MZI, and the silicon nitride rib waveguide. (b) Layout of the 10 MZIs showing the MZI routes as well as the LED positions and metal [17].

proposed design, the incoming light was split into two arms by the waveguide. One of the arm was exposed to the analyte and the other arm was used as reference. The interference pattern was detected on at the point of recombination of the two arms due to the deliberately induced asymmetry. Subsequent to interaction of the analyte with the evanescent field of the waveguide at the sensing window, a phase shift was introduced due to variation in the refractive index. Performance of the proposed sensor platform in terms of signal-to-noise-ratio (SNR) and absolute response is compared with the commercial quartz crystal microbalance with dissipation (QCM-D). The aMZI proved itself dominated over the QCM-D due to measurement capability streptavidin binding with no need of the added complication of hydrodynamically coupled water which allow the elucidation of absolute protein adsorption. Also the aMZI presented 200 times good SNR and therefore offered a relatively lower limit of detection.

The operation of a versatile and sensitive integrated optical MZI biosensor with three-guide coupler at the output was demonstrated by B. J. Luff et al. as shown in **Figure 7**. The interferometric devices were designed by Ag⁺–Na⁺ ionexchange in glass substrates. The chemical modification of the waveguide surface of the interferometer made possible the detection of the biochemical species. The waveguide were designed in BGG36 glass with refractive index about 1.6 at 786 nm by Ag⁺–Na⁺ ion-exchange. Photolithographically patterned Ti film was used as the masking material with

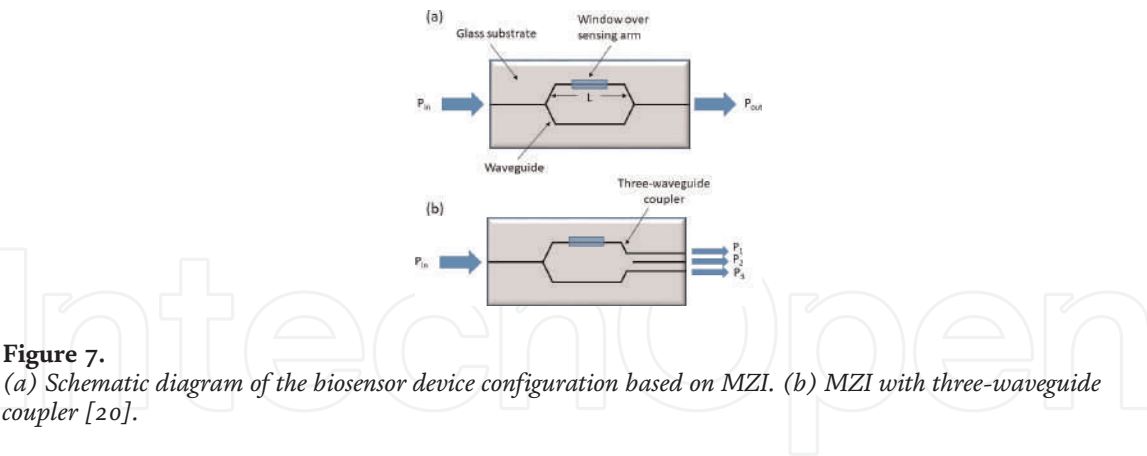


Figure 7. (a) Schematic diagram of the biosensor device configuration based on MZI. (b) MZI with three-waveguide coupler [20].

opening width of 1 μm . The fabricated device was characterized by different concentrations of sucrose solutions to vary the superstrate index. For building up multilayers of protein over the sample surface, a high affinity interaction between vitamin biotin and protein streptavidin base system was used. The refractive index and thickness of the protein multilayer system was calculated reproducibly based on waveguide model.

3.2 Fabry–Pérot interferometer

Fabry–Pérot interferometer (FPI) also called etalon is based on an optical cavity made from two parallel reflecting surfaces. The interferometer is named after Charles Fabry and Alfred Perot for their invention in 1899. The parallel reflecting surfaces of the FP cavity is separated by a distance ‘d’ which allows the transmission of infinite number of parallel to each other as shown in **Figure 8**. A sharp constructive interference can be recorded when these parallel beam superimposed with each other. Free spectral range (FSR) analysis can be used to calculate the separation between the reflective ends of the cavity from refractive index information of a known medium. The spacing between the two reflective surfaces can be calculated from the FSR from refractive index of a known medium, as follow;

$$\text{FSR} = \Delta \nu = \nu_{m+1} - \nu_m = \frac{c}{2nd\cos\theta} \tag{20}$$

Where, ν is the frequency at which transmission of maximum intensity occurs, m determines an integral order of transmission peaks, θ is the angle of maximum transmission, d is the separation between the end reflective cavity surfaces and n is the index of refraction of a specific medium. FP interferometers are highly sensitive for the detection of OAMs therefore, mostly applied by the researchers in the literature.

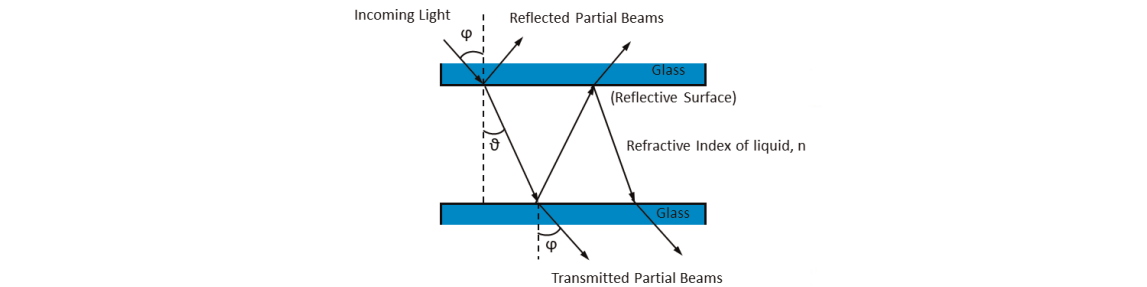


Figure 8. Schematic diagram of the principle of the Fabry-Perot interferometer etalon. Basic structure of cavity [21].

The FPI is highly sensitive to any perturbation causing a variation in the optical path length between its two reflective mirrors as presented in **Figure 9**. Due to its compact size, high sensitivity and fast response, the FPI is applied for different physical parameters sensing, biosensing, gas sensing, current and magnetic field detection etc. [23]. FP etalons based optical sensors provide an efficient label-free biosensing capability with enhanced sensitivity. The biosensing of etalon is measured in terms of absorption or phase shift subsequent to interference between the reflected light beams from the two reflecting surfaces in its cavity [24–29].

G. Allison et al. investigated an efficient FP cavity coupled surface plasmon photodiode for electrical label-free biomolecular sensing [30]. The surface plasmonic sensor was developed inside a photovoltaic cell. The information of solutions containing biomolecules was extracted from its refractive indices in the form of electronic signal generated subsequent to incident light. The resultant photocurrent was enhanced due to surface plasmon mode coupling with the FP modes inside the photovoltaic cell due to its absorbing layer. An optically transparent substrate with special ability for surface plasmon resonance (SPR) was replaced by a silicone layer of semi-transparent optical nature. With the help of this mechanism, an absorbing layers was sandwiched between a metallic layer and an optically transparent conducting electrode. Photocurrent was caused as a result of incident light due to built-in

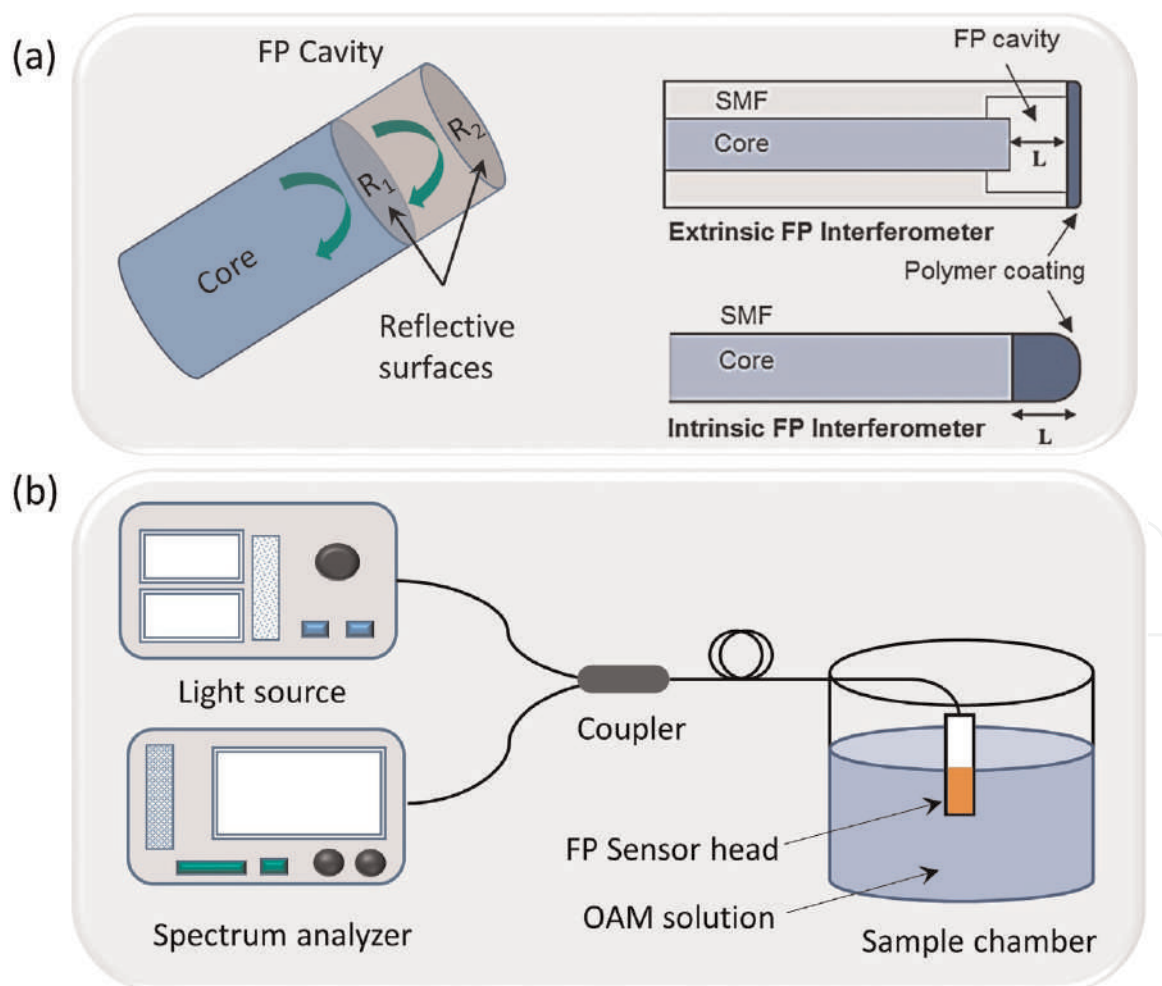


Figure 9.
 (a) FP interferometer having reflective surfaces with reflectivity of R_1 and R_2 , respectively. Examples of intrinsic and extrinsic FP interferometers. (b) Schematic representation of the FP based experimental setup employed for detection of gaseous biomolecules [22].

potential of fabricated device in a similar nature to that of photovoltaic cell. The surface plasmon was excited in the metal layer and generated the photocurrent simultaneously by illuminating a thin silicon layer by a visible light with single wavelength at a resonant angle. The photocurrent was reduced drastically by surface plasmon due to disruption of the distribution of electric field in the silicone layer. The mechanism were further enhanced by the silicone layer as an optical FP cavity to produce the FP modes which were coupled with the plasmon mode. The mechanism was confirmed by the simulation of the distribution of electric field which was further confirmed experimentally by electric detection of mode and resultantly the variations in the refractive index and the protein – protein interactions were measured.

A microfluidic optical sensor integrated with FP etalon geometry was investigated for detection of concentrations of different biochemical species in solution by K. E. You et al.. The concentration information were extracted in terms of the refractive index variation with concentration with high accuracy and sensitivity. The FP cavity was fabricated from a liquid channel with two partially reflected Ag/SiO₂ reflective surfaces. The refractive index dependent interference peaks were achieved in the transmission spectra subsequent to transmission of light through the fluid channel. Concentrations of different biomolecules, i.e., glucose, potassium chloride and sodium chloride were calculated from their refractive indices in terms of a shift in the position of maxima of wavelength of the interference peaks in the transmission spectra. The devised optical sensor shown a linear response with good accuracy. Sensitivities of 10^{-3} , 1.4×10^{-3} and 1.8×10^{-3} refractive indices per percent of glucose, KCl and NaCl, respectively were obtained. Schematic diagram of the investigated FP cavity based optical sensor and its response to the optically active glucose sample was shown in Figure 10.

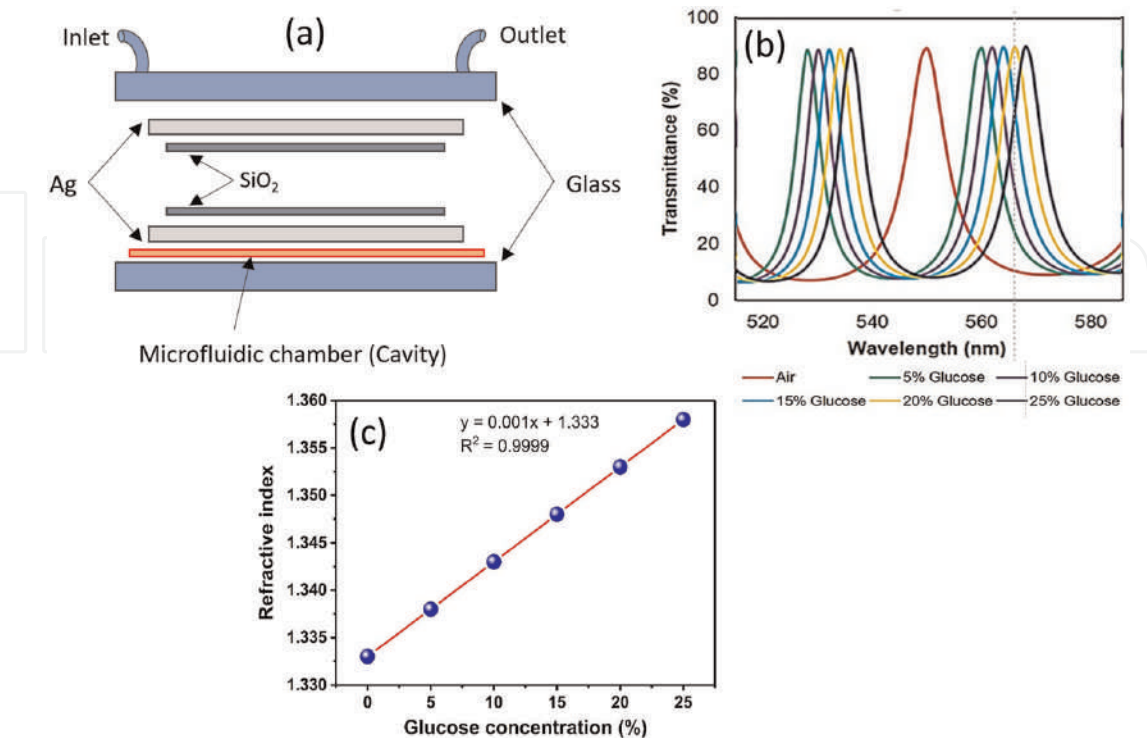


Figure 10. Schematic diagram of the devised modified microfluidic Fabry-Perot etalon (a) 2D view, (b) simulation (c) refractive index vs. glucose concentration (%) [21].

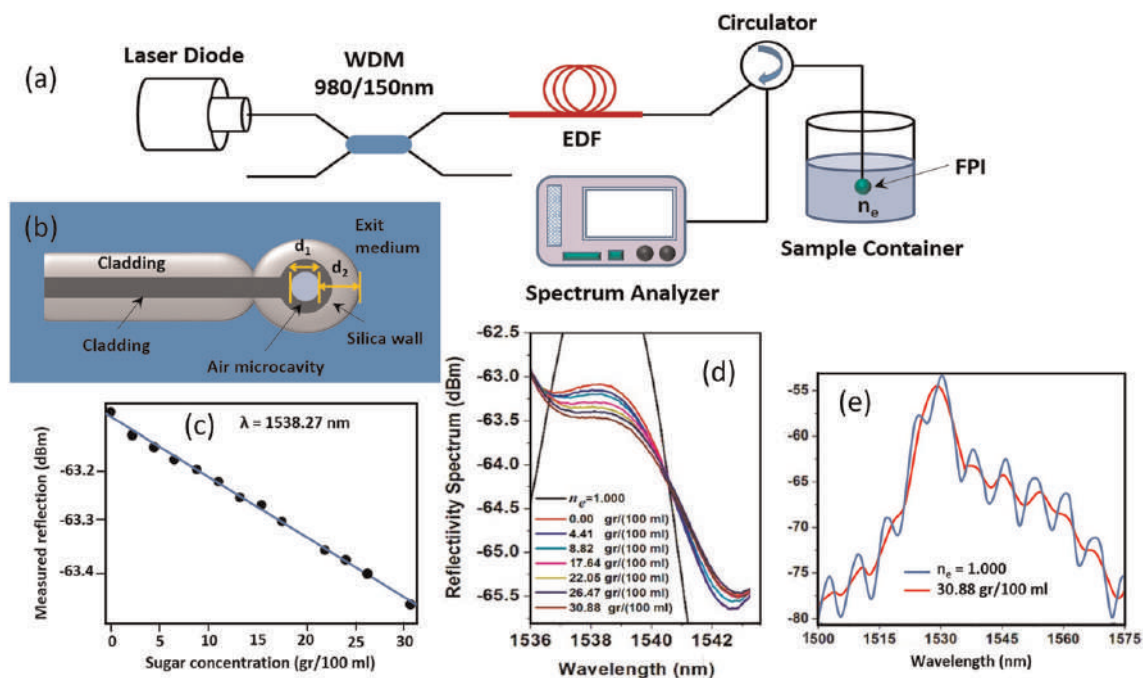


Figure 11.
 (a) Schematic diagram of the experimental setup for MFPI based sugar concentration sensing, (b) schematic view of the fabricated MFPI, (c) reflected energy and the refractive index of the exit medium at $\lambda = 1538.27$ nm as a function of the sugar concentration (d) measured reflected power spectra for different sugar concentrations and (e) enlarged view of the spectra [31].

A micro Fabry-Pérot interferometer (MFPI) was designed and developed for quantitative determination of sugar in a transparent solutions by G. Chavez et al. as shown in **Figure 11(a)**. The MFPI was developed in the form of a micro bubble made of a hollow core photonic crystal fiber (PCF) as shown in **Figure 11(b)**. The cavity was fabricated by splicing of a segment of PCF to a single mode fiber (SMF) by a conventional arc fusion splicer which form an air MFPI. The fabricated MFPI then acted like an optical cavity having two reflecting surface of different refractive indices separated by a distance d . The erbium doped fiber (EDF) was illuminated by 200 mW laser diode with 980 nm wavelength with the help of wavelength division multiplexer (WDM). Output light from EDF was incident on the MFPI subsequent to passing through a three-port circulator. The reflection from MPI was guided towards optical spectrum analyzer (OSA) by port three of the circulator. The MFPI was immersed inside a sugar solution filled cuvette and the reflected interference patterns were recorded at different concentrations of sugar solution in the range 0–30.88 g/100 ml. The contrast of the interference fringes decreases with increased in the sugar concentration in solution as illustrated in **Figure 11(d)**. The predicted results from simulation were also experimentally confirmed with good agreement. The reflected optical power was directly decreased with increase in the concentration and resultant refractive index of solution with sensitivity of -0.0123 dBm/(g/100 ml) at 1538.27 nm wavelength.

J. Martini et al. also proposed a glucose concentration sensor in interstitial fluids based on a small size double-chamber FP etalon. One of the FP chamber of the proposed sensor was used as reference to overcome the effect of ambient temperature variations. The 400 μ m etalon cavity was filled with water – glucose solution which had FSR of 680 pm in response to the normal incident light of wavelength 850 nm. A wavelength shift of ~ 1 pm was produces per 1 mg/dl of the optically active analyte (glucose). The light beam from an SM vertical cavity surface emitting laser (VCSEL,

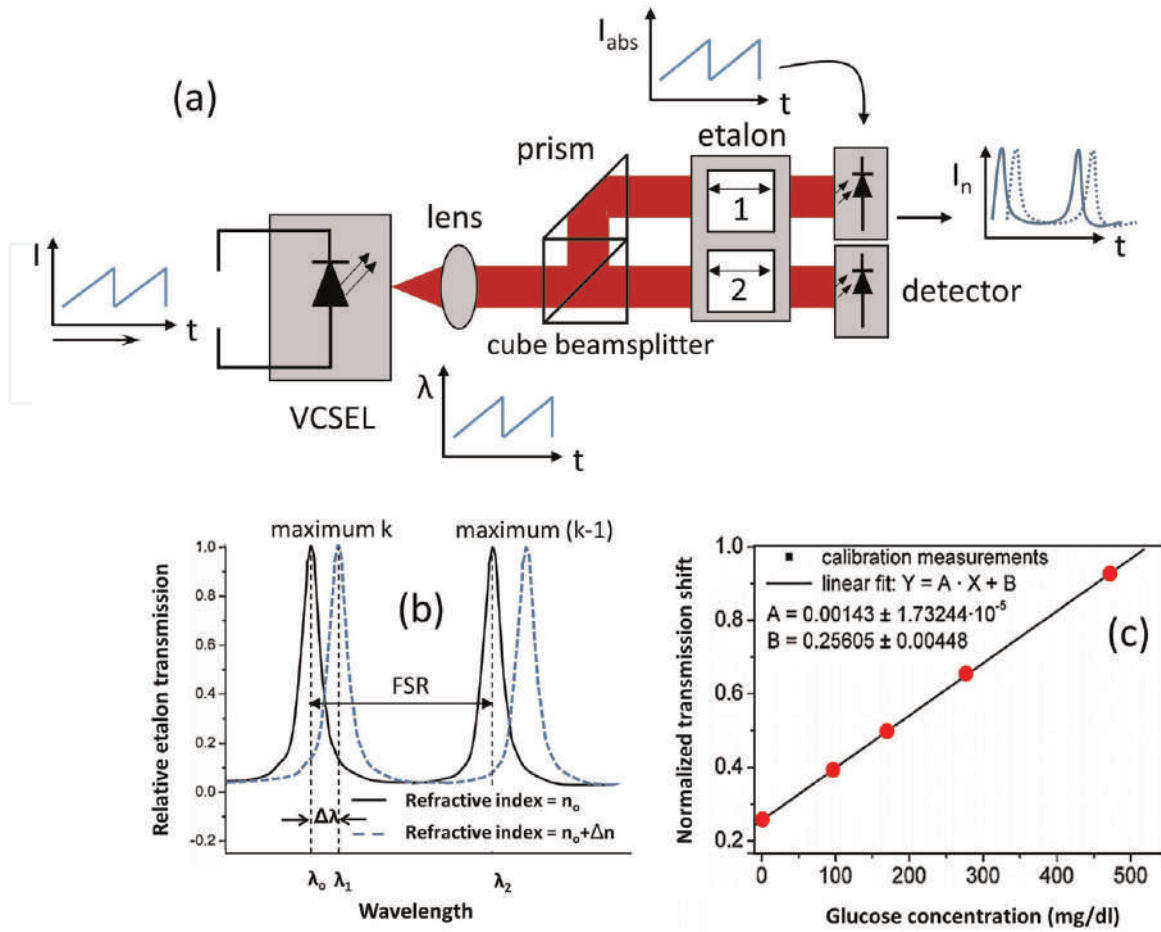


Figure 12.

(a) Schematic diagram of the experimental setup of the double-chamber FP etalon (b) spectral position of FP modes for two different refractive indices (c) calibration curve of the refractive index with varied concentration of glucose [32].

850 nm) was guided towards 50/50 beam splitter and was incident on one of the FP chamber subsequent to proper collimation. The perpendicular half of the beam was redirected into the other FP chamber with the help of a prism. The transmitted light signal from FP chamber were recorded by PIN photodiodes with two active segments as shown in **Figure 12**. Difference in the refractive indices of the two etalon chambers produced a phases in the transmitted optical signals. The proposed optical sensor was studied in the range 0–700 mg/dl of glucose concentration with precision of ± 2.5 mg/dl. The temperature compensation was confirmed in the range 32–42°C.

3.3 Sagnac interferometer

In the Sagnac interferometer, the light beam is split to follow the same optical path but in opposite directions in the form of a closed loop. The beams get interference upon returning back to the point of entry. In the case of optical fiber Sagnac interferometer, a section of birefringent fiber is splices to the loop which causes interference between the counter propagating light beams.

A Sagnac interferometer based optical sensor system was designed, developed and demonstrated by T. Kumagai et al. for quantitative analysis of glucose in a solution. The optical rotation proportion to concentration of glucose concentration was measured in a Sagnac loop from a phase difference introduced between the clockwise

(CW) and counter clockwise circularly polarized light. The proposed optical sensor was composed of a Sagnac interferometer made from a polarization maintaining fiber (PMF) and other optical components to avoid the unwanted sources of noise due to different reasons. A coherent light of wavelength 840 nm from a super luminescent diode was transmitted in the sensor system. Two orthogonal mode of polarizations with a minor difference in their propagations constants were transmitted in the interferometer. The ambient sources of noise those were temperature variations and external vibrations may vary the zero level of the output signal which were controlled by fabricating the interferometer from PMF. A quarter-wave retarder was used to convert the linearly polarized light into circularly polarized light which was subsequently passed through a low birefringence span SMF or in free space. The interference signal achieved from recombination of CCW and CW lights was confirmed from the output of a preamplifier and was physically observed on an oscilloscope. The polarization measurement system (polarimeter) was checked by measuring the phase difference with the help of Faraday effect optical rotation measurement setup. In this regard, current was applied to a 1300-turn copper coil and a span fiber was a wounded around the coil. Concentration of glucose was measured from the degree of optical rotation using Biot's law as shown in Eq. (1). The phase difference analysis was performed in a 1 dm long measurement cell. The specific rotation of +51.6 and - 91.2 were measured for glucose and fructose respectively which were close to their physical properties. To make the sensor suitable for practical applications, the active length of the measurement cell was reduced to about 2 mm and the resolution of the sensor was monitored. A trial based noninvasive measurement with human body was performed by skin webbing between fingers. The resultant interference between CCW and CW lights was investigated. The skin webbing caused a bias in the interference signal which was observed in the form of noise due to a phase difference between CCW and CW light. A resolution of 1 mg/dl was achieved for glucose concentration and 0.5 mdeg resolution of optical rotation was detected for the devised sensor (**Figure 13**).

An optical polarimetry based Sagnac interferometry technique was investigated for noninvasive glucose sensing by A. M. Winkler et al. [34]. A phase shift in the interference fringes of the Sagnac interferometer was detected in a glucose solution as a representative OAM. The proposed method was linked with the sugar detection from the aqueous humor of human eye. The interferometer was simulated such that the counter propagating beams in which one of them passed through an optically active sample caused a difference in the optical path traversing. The effect was due to a difference in the refractive indices of the left and right circularly polarized beams.

A compact PCF Sagnac interferometer based glucose sensor was introduced by G. Ann et al. [35]. A light signal from a broadband light source was launched in a 3 dB coupler and split into two beams.. A Saganac loop was mainly comprised of a polarization controller and PCF spliced with an SMF. The splitted beams counter propagated and interfered with an accumulated phase difference when passed through the PCF. The interference signal was effected greatly by the phase difference between the two orthogonal guided modes of PCF. A similar trend of phase birefringence was observed when the wavelength was varied in the range 1000–2000 nm with a gradual decrease in the maxima of the curve with increase in the glucose concentration. The nature of the devised sensor was analyzed between 15 cm to 40 cm. It was observed that the response of the sensor was highly sensitive to the PCF length. A prominent interference peaks were observed between 1050 nm to 2000 nm. The interference

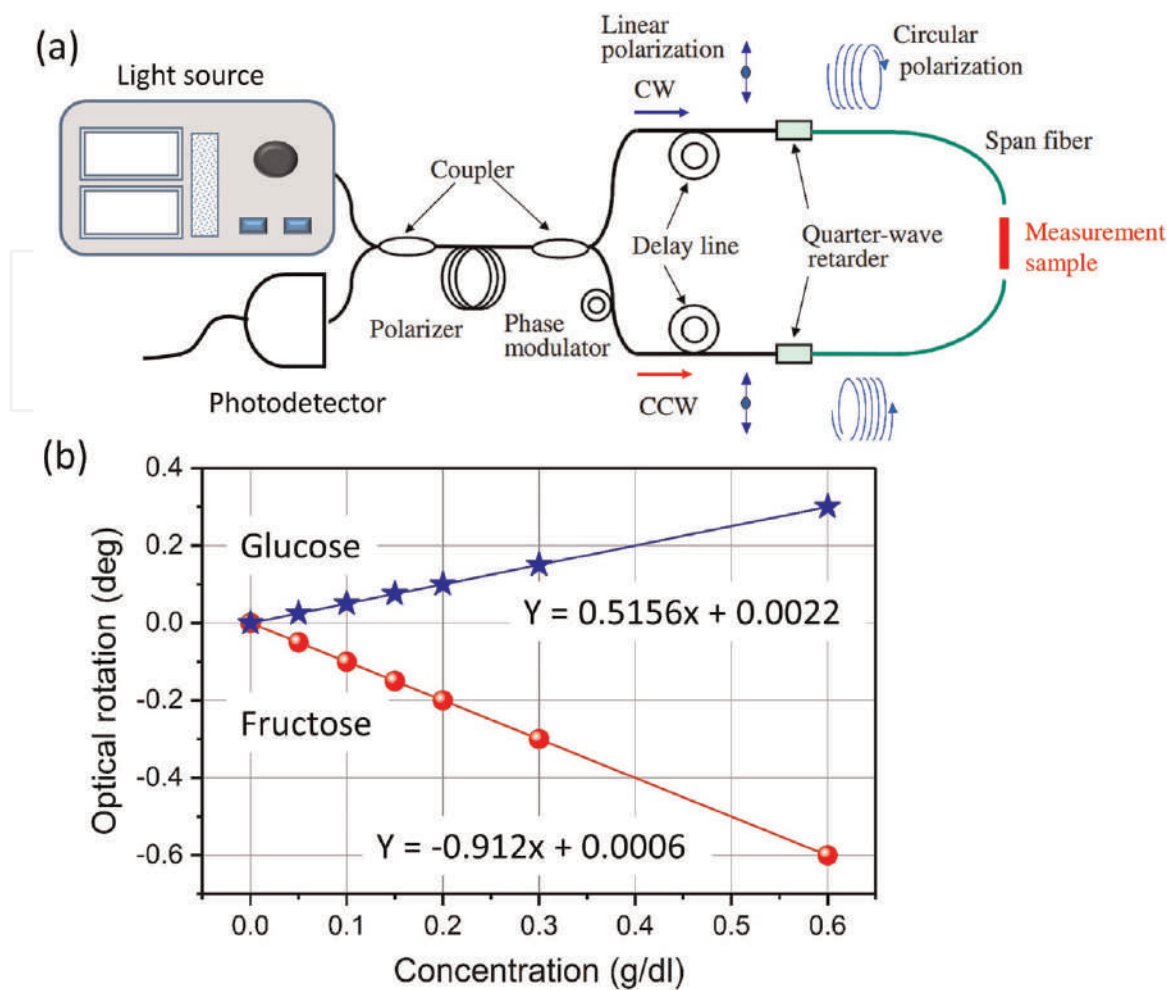


Figure 13. (a) Configuration of optical rotation measurement system with a Sagnac interferometer. (b) Concentration dependent optical rotation of sugar samples [33].

signatures becomes highly sensitive with good SNR for 20 cm PCF length. An average sensitivity of 0.76 mg/dL of glucose solution in water was recorded which is lower than 70 mg/dl of hypoglycemia episodes. The sensor was designed for effective sensing of glucose level in the patients with hypoglycemia.

3.4 Michelson interferometer

In this type of interferometer, a coherent light beam is split into two by a beam splitter. Each of the two beams are reflected back and recombines at the same beam splitter to get interference pattern. Although, the Michelson interferometer has good potential for the detection of OAMs but rarely applied due to its relatively complex optical arrangements. L. K. Chin reported a droplet Michelson interferometer for biochemical and protein detection. The interferometer was fabricated in the form of on-chip liquid grating as schematically shown in **Figure 14(a)**. A branch of the interferometer was spared for injection of two immiscible liquids. A T-junction was developed for the formation of the liquid grating. The other branch with microchannel was filled with immersion oil which caused a phase shift due to optical path difference produced in the paths of light transmitted through the core and the cladding. A buffer solution was injected in the third branch to measure its refractive index. An optical fiber was

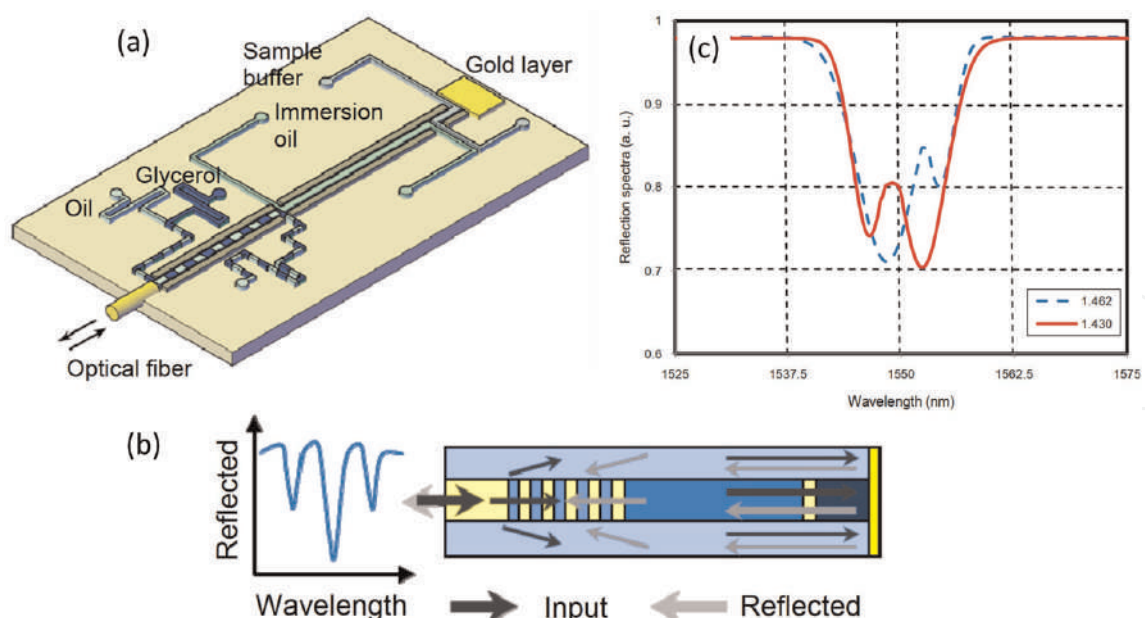


Figure 14. Schematic illustrations of (a) the droplet Michelson interferometer and (b) the physics model of Michelson interferometer (c) reflection spectra of liquid grating Michelson interferometer [36].

aligned with one end of the microchannel for input/output light detection and the other end was coated with a gold film to use it as end mirror. The light was coupled from core to the cladding with the help of liquid grating. In the interferometer, the second and third branches of the microchannel was used to propagate the light which was reflected back by the gold layer which caused an optical path difference. An interference pattern was observed with attenuation band when both the light signals recombines in the core subsequent to passing through the liquid grating as shown in **Figure 14(b)**. The microchip was fabricated in polydimethylsiloxane (PDMS) using lithography. Sputtering technique was applied to coat the sidewall of the PDMS edge. The PDMS slab with the pattern was attached with the unpatented PDMS slab using plasma bonding. The broadband light was coupled by an optical circulator with the optofluidic chip. The reflection from the optofluidic interferometer was detected by an OSA. The immersion oil and glycerol with refractive indices 1.462 and 1.420, respectively were used as carrier and dispersed flow, respectively. Reflection from the devised interferometer for different buffers with distinct refractive indices was recorded by the spectrum analyzer as shown in **Figure 14(c)**. Two distinct attenuation peaks were observed in the overall attenuation band at slightly different positions and intensities.

4. Conclusion

In this study, different interferometric optical sensors employed for the detection and quantification of OAMs are briefly reviewed (**Table 1**). The working principle, design and the important performance parameters including working range, sensitivity, and limit of detection were discussed in detail. Different materials analyzed in the sensors were outlined with special focus on sugar and protein being a representative OAMs. Two different interferometric arrangements, i.e., free space and optical fiber based optical sensors were discussed. It was

Interferometer	Characterized material	Dynamic range	Sensitivity	Limit of detection	Reference
Mach-Zehnder	Protein	50–1000 nm	2000 nm/RIU	—	[11]
	Glucose	625 mg/ml	−2.36°/ml	25.5 mg/ml	[14]
	Fructose	922 mg/ml	−1.31°/ml	37.5 mg/ml	
	Sucrose	—	4.413 nm/RUI	—	[15]
	Glucose/protein	—	—	10 mM	[18]
	Protein	—	0.4 rads/ng/mm ²	2 pg/mm ²	[20]
	Glucose	0–25%	0.001 RUI/%	10-5 RUI	[21]
Fabry–Pérot	glycerol	0–50%	1.5 μA/mRIU	10 pg/ml	[30]
	Sugar	0–30.88 g/100 ml	−0.0123 dBm/(g/100 ml)	—	[31]
	Glucose	0–700 mg/dl	2.5 mg/dl		[32]
Sagnac	Glucose	0–0.6 g/dl	0.5156 deg/(g/dl)	1 mg/dl	[33]
	Fructose	0–0.6 g/dl	0.9120 deg/(g/dl)	—	
	Glucose	0–500 mg/dl	—	—	[34]
	Glucose	0–120 g/l	2.63 nm/g/l	0.76 mg/dl	[35]

Table 1.
Comparison of different OAMs analyzed by different interferometric arrangements.


concluded that optical fiber based interferometry has mind blowing potential for highly precise sensing of OAMs with good sensitivity and can be applied in industrial and research and development applications.

Author details

Rahim Ullah*, Raja Yasir Mehmood Khan and Muhammad Faisal
National Institute of Lasers and Optronics College, Pakistan Institute of Engineering and Applied Sciences, Islamabad, Pakistan

*Address all correspondence to: rahimullahphysics28@gmail.com

IntechOpen

© 2022 The Author(s). Licensee IntechOpen. This chapter is distributed under the terms of the Creative Commons Attribution License (<http://creativecommons.org/licenses/by/3.0>), which permits unrestricted use, distribution, and reproduction in any medium, provided the original work is properly cited. 

References

- [1] de Souza RR, Fernandes DD d S, Diniz PHGD. Honey authentication in terms of its adulteration with sugar syrups using UV-vis spectroscopy and one-class classifiers. *Food Chemistry*. 2021;**365**:130467. DOI: 10.1016/J.FOODCHEM.2021.130467
- [2] Chen C, Jiang Y, Kan J. A noninterference polypyrrole glucose biosensor. *Biosensors & Bioelectronics*. 2006;**22**(5):639-643. DOI: 10.1016/J.BIOS.2006.01.023
- [3] Islam MK, Sostaric T, Lim LY, Hammer K, Locher C. A validated method for the quantitative determination of sugars in honey using high-performance thin-layer chromatography. *JPC – Journal of Planar Chromatography – Modern TLC*. 2020;**33**(5):489-499. DOI: 10.1007/S00764-020-00054-9
- [4] Khalil SKH, Kamil M. Application of FT-IR spectroscopy for rapid and simultaneous quality determination of some fruit products environmental microbiology view project drug delivery system view project. *Natural Science*. 2011;**9**(11):21-31
- [5] And JFDK, Downey G. Detection of sugar adulterants in apple juice using Fourier transform infrared spectroscopy and Chemometrics. *Journal of Agricultural and Food Chemistry*. 2005;**53**(9):3281-3286. DOI: 10.1021/JF048000W
- [6] Guven B, Durakli-Vellioglu S, Boyaci İH. Rapid identification of some sweeteners and sugars by attenuated Total reflectance-Fourier transform infrared (ATR-FTIR), near-infrared (NIR) and Raman spectroscopy. *Gıda*. 2019;**44**(2):274-290. DOI: 10.15237/GIDA.GD18119
- [7] Xu Y et al. Raman spectroscopy coupled with chemometrics for food authentication: A review. *TrAC Trends in Analytical Chemistry*. 2020;**131**:116017. DOI: 10.1016/J.TRAC.2020.116017
- [8] Soni M. A review on the measurement of optical activity by using a Polarimeter. *Journal of Pharmacognosy and Phytochemistry*. 2019;**8**(2):358-360
- [9] Pokrzywnicka M, Koncki R. Disaccharides determination: A review of analytical methods. *Critical Reviews in Analytical Chemistry*. 2017;**48**(3):186-213. DOI: 10.1080/10408347.2017.1391683
- [10] Tan C-T, Wang C, He J-N, Chiu M-H. Phase sensitive optical rotation measurement using the common-path heterodyne interferometry and a half-wave plate at a specific azimuth angle. *OSA Continuum*. 2021;**4**(1):239-251. DOI: 10.1364/OSAC.415766
- [11] Goodwin MJ, Besselink GAJ, Falke F, Everhardt AS, Cornelissen JJLM, Huskens J. Highly sensitive protein detection by asymmetric Mach-Zehnder interferometry for biosensing applications. *ACS Applied Bio Materials*. 2020;**3**(7):4566-4572. DOI: 10.1021/ACSABM.0C00491
- [12] Buiarelli F, Di Filippo P, Pomata D, Riccardi C, Rago D. Determination of sugar content in commercial fruit juices by Refractometric, volumetric and chromatographic methods. *Journal of Nutritional Therapeutics*. 2016;**5**(3):75-84. DOI: 10.6000/1929-5634.2016.05.03.3
- [13] Handapangoda, Chintha C, Premaratne M, Yeo L, Friend J. Laguerre Runge-Kutta-Fehlberg method for simulating laser pulse propagation in

biological tissue. *IEEE Journal of Selected Topics in Quantum Electronics*. 2008;**14**(1):105-112. DOI: 10.1109/JSTQE.2007.913971

[14] Calixto S, Martinez-Ponce G, Garnica G, Figueroa-Gerstenmaier S. A Wavefront division Polarimeter for the measurements of solute concentrations in solutions. *Sensors*. 2017;**17**(12):2844. DOI: 10.3390/S17122844

[15] Razak HA, Sulaiman NH, Haroon H, Mohd Zain AS. A fiber optic sensor based on Mach-Zehnder interferometer structure for food composition detection. *Microwave and Optical Technology Letters*. 2018;**60**(4):920-925. DOI: 10.1002/MOP.31072

[16] Kitsara M, Raptis I, Misiakos K, Makarona E. Broad-band mach-zehnder interferometry as a detection principle for label-free biochemical sensing. *Proceedings of IEEE Sensors*. 2008: 934-937. DOI: 10.1109/ICSENS.2008.4716594

[17] Psarouli A et al. Monolithically integrated broad-band Mach-Zehnder interferometers for highly sensitive label-free detection of biomolecules through dual polarization optics. *Scientific Reports*. 2015;**5**(1):1-11. DOI: 10.1038/srep17600

[18] Kee JS, Kim KW, Park MK, Liu Q, Gu Z. Single-channel Mach-Zehnder interferometric biochemical sensor based on two-lateral-mode spiral waveguide. *Optics Express*. 2014;**22**(23): 27910-27920. DOI: 10.1364/OE.22.027910

[19] Bruck R, Melnik E, Muellner P, Hainberger R, Lämmerhofer M. Integrated polymer-based Mach-Zehnder interferometer label-free streptavidin biosensor compatible with injection molding. *Biosensors &*

Bioelectronics. 2011;**26**(9):3832-3837. DOI: 10.1016/J.BIOS.2011.02.042

[20] Luff BJ, Wilkinson JS, Piehler J, Hollenbach U, Ingenhoff J, Fabricius N. Integrated optical Mach-Zehnder biosensor. *Journal of Lightwave Technology*. 1998;**16**(4):583-592

[21] You KE, Uddin N, Kim TH, Fan QH, Yoon HJ. Highly sensitive detection of biological substances using microfluidic enhanced Fabry-Perot etalon-based optical biosensors. *Sensors and Actuators B: Chemical*. 2018;**277**:62-68. DOI: 10.1016/J.SNB.2018.08.146

[22] Khan S, Le Calvé S, Newport D. A review of optical interferometry techniques for VOC detection. *Sensors and Actuators A: Physical*. 2020; **302**:111782. DOI: 10.1016/J.SNA.2019.111782

[23] Huang YW, Tao J, Huang XG. Research Progress on F-P interference—Based Fiber-optic sensors. *Sensors*. 2016;**16**(9):1437. DOI: 10.3390/S16091424

[24] Que L, Giorno R, Zhang T, Gong Z. A nanostructured Fabry-Perot interferometer. *Optics Express*. 2010; **18**(19):20282-20288. DOI: 10.1364/OE.18.020282

[25] Dohi T, Matsumoto K, Shimoyama I. The optical blood test device with the micro Fabry-Perrot interferometer. 17th IEEE International Conference on Micro Electro Mechanical Systems. Maastricht MEMS 2004 Technical Digest. IEEE, 2004. pp. 403-406

[26] Bhatia V et al. Optical fibre based absolute extrinsic Fabry - Pérot interferometric sensing system. *Measurement Science and Technology*. 1996;**7**(1):58. DOI: 10.1088/0957-0233/7/1/008

- [27] Majchrowicz D, Hirsch M, Wierzbna P, Bechelany M, Viter R, Jędrzejewska-Szczerska M. Application of thin ZnO ALD layers in Fiber-optic Fabry-Pérot sensing interferometers. *Sensors*. 2016;**16**(3):416. DOI: 10.3390/S16030416
- [28] Yeatman EM, Caldwell ME. Surface-plasmon spatial light modulators based on liquid crystal. *Applied Optics*. 1992; **31**(20):3880-3891. DOI: 10.1364/AO.31.003880
- [29] Chiang KS, Liu WJ, Liao X, Rao YJ, Ran ZL. Laser-micromachined Fabry-Perot optical fiber tip sensor for high-resolution temperature-independent measurement of refractive index. *Optics Express*. 2008; **16**(3):2252-2263. DOI: 10.1364/OE.16.002252
- [30] Allison G et al. A Fabry-Pérot cavity coupled surface plasmon photodiode for electrical biomolecular sensing. *Nature Communications*. 2021;**12**(1):1-7. DOI: 10.1038/s41467-021-26652-7
- [31] Chavez G, Dinora A, Contreras C, Martin, Daniel JV. Sugar concentration sensor based on a micro Fabry-Perot interferometer. *ECORFAN-Journal*. 2017;**1**(2):16-21
- [32] Martini J, Kiesel P, Roe JN, Bruce RH. Glucose concentration monitoring using a small Fabry-Pérot etalon. *Journal of Biomedical Optics*. 2009;**14**(3):034029. DOI: 10.1117/1.3153848
- [33] Kumagai T, Tottori Y, Miyata R, Kajioka H. Glucose sensor with a Sagnac interference optical system. *Applied Optics*. 2014;**53**(4):720-726. DOI: 10.1364/AO.53.000720
- [34] Winkler AM, Bonnema GT, Barton JK. Optical polarimetry for noninvasive glucose sensing enabled by Sagnac interferometry. *Applied Optics*. 2011;**50**(17):2719-2731. DOI: 10.1364/AO.50.002719
- [35] Ann G, Li S, An Y, Wang H, Zhang X. Glucose sensor realized with photonic crystal fiber-based Sagnac interferometer. *Optics Communication*. 2017;**405**:143-146. DOI: 10.1016/J.OPTCOM.2017.08.003
- [36] Chin LK, Lim CS, Liu AQ. A droplet Michelson interferometer for biochemical and protein analysis. *Thirteenth International Conference on Miniaturized Systems for Chemistry and Life Sciences*. Jeju. Korea. November 1–5. 2009. pp. 743-745

We are IntechOpen, the world's leading publisher of Open Access books Built by scientists, for scientists

6,300

Open access books available

171,000

International authors and editors

190M

Downloads

Our authors are among the

154

Countries delivered to

TOP 1%

most cited scientists

12.2%

Contributors from top 500 universities



WEB OF SCIENCE™

Selection of our books indexed in the Book Citation Index
in Web of Science™ Core Collection (BKCI)

Interested in publishing with us?
Contact book.department@intechopen.com

Numbers displayed above are based on latest data collected.
For more information visit www.intechopen.com



Interferometric Gravitational Wave Detectors

Carlos Frajuca

Abstract

The existence of gravitational waves is an important proof of Einstein's theory of general relativity and took 100 years to be achieved using optical interferometry. This work describes how such a detector works and how it can change the way of seeing the Universe. Kilometers size laser interferometers are being built around the world in the way to make gravitational astronomy; detectors already built in the United States, Italy, and Japan will join efforts with detectors built in Japan and India and provide humanity with the means to see gravitational interactions of black holes and neutron star. Interactions, without these detectors, will be forever out of our sight.

Keywords: interferometric, gravitational waves, gravitational wave detectors, interferometric gravitational wave detectors, gravity

1. Introduction

Gravitational waves are ripples in the curvature of spacetime that propagate like waves, traveling outward from the source; they travel at the speed of light (299,792,458 m/s) and squeeze and stretch anything in their path as they pass. Do not confuse it with gravity waves that are waves generated when the force of gravity in a fluid medium or, when it is the case, at the interface between two different media, tries to restore equilibrium, as an example of these waves there are the wind waves on the interface between the atmosphere and the ocean.

Predicted in 1916 [1, 2] by Albert Einstein based on his theory of general relativity, [3] and detected in 2015, gravitational waves transport energy in the form of gravitational radiation, oscillation of spacetime itself. This theory predicts that the presence of mass causes spacetime to warp. When massive objects move around themselves, this curvature is altered, sending ripples of gravitation out of the universe carrying unbelievable amounts of energy. As these sources are very distant by the time, these disturbances catch up with us; they are almost imperceptible because they are weaker and gravitational waves interact very weakly with matter. Because of that, it was only a century after Einstein's prediction that scientists developed a sensitive enough detector—a Laser Interferometer Gravitational-Wave Detector, some kilometers long interferometer and were able to confirm the existence of gravitational waves [4].

The existence of gravitational waves is also a consequence of the Lorentz covariance of general relativity since it brings the concept of a finite speed of propagation of gravity.

Gravitational waves did not exist in the Newtonian theory of gravitation, which postulates that physical interactions propagate at infinite speed.

There was already indirect evidence of gravitational waves before its first direct detection. Measurements of the Hulse-Taylor binary system suggested that gravitational waves were more than a hypothetical concept. This system is one of the potential sources of detectable gravitational waves. These potential sources include binary compact star systems composed of white dwarfs, neutron stars, and black holes.

One way of thinking about gravitational radiation is as the messenger that carries information about changes in gravitational fields that attract one thing to another [5].

Several gravitational wave observatories (detectors) are under construction or in operation around the world [6]. In 2017, the Nobel Prize in Physics was awarded to Rainer Weiss, Kip Thorne, and Barry Barish for their role in detecting gravitational waves [7]. In these gravitational wave detectors and previous ones, the use of interferometry was essential for the operation of such a detector.

2. Some history

The possibility of gravitational waves was discussed in 1893 by Oliver Heaviside using the analogy between the inverse square law of distance in gravitation and electricity [7]. In 1905, Henri Poincaré proposed for the first time the existence of gravitational waves, which emanated from accelerated bodies and propagated at the same speed of light, this is dictated by the transformations of Lorentz [8] and implies an analogy that, accelerating electric charges produce electromagnetic waves, accelerating masses must emanate gravitational waves. When publishing his theory of gravitation (the general theory of relativity) in 1915, Einstein did not agree with Poincaré's proposal, as in his theory there are not gravitational dipoles, essential for the emission in the electromagnetism theory. However, based on a weak field approximation, he concluded that there should be three kinds of gravitational waves (named by Hermann Weyl as longitudinally-longitudinally, transversely-longitudinally, and transversely-transverse).

These approximations made by Einstein were criticized by several researchers and even Einstein had doubts. In 1922, Arthur Eddington wrote a paper entitled: "The propagation of gravitational waves" [8], in which he showed that two of the three types of waves proposed by Einstein were only mathematical artifacts produced by the system of coordinates and they were not really waves. This also cast doubt on the physicality of the third type (transversely transverse); however, Eddington proved that these would travel at the speed of light in all coordinate systems, so he did not rule out their existence.

In 1956, Felix Pirani corrected the confusion caused by the use of several coordinate systems by reformulating gravitational waves as the manifestation of the Riemann tensor observables. The Pirani work was ignored at that time mainly because the scientific community was concerned with another issue of whether gravitational waves could transport energy. This question was solved by Richard Feynman using a thought experiment presented at the first conference for General Relativity in 1957 known as the Chapel Hill Conference. His argument, known as the sticky bead argument, presents that: if a gravitational wave passes orthogonally to the beaded rod (a rod if some bead), the effect of it is to deform the bead and the rod, but as the rod is longer, the bead moves beads over the rod; this movement causes friction and then heat, which meant the passing gravitational wave would have energy. Afterward,

Hermann Bondi (who was skeptical of the existence of gravitational waves) published a more complete version of this argument.

After this conference, the scientific community took the existence of gravitational waves more seriously. Joseph Weber began to design and build a gravitational wave detector. It was the start of many gravitational wave detectors that are called Weber bars. Weber claimed to have detected gravitational waves in 1969 and 1970, the signals coming from the Galactic Center [9]. However, the high detection frequency quickly cast doubt on the validity of his observations, as the Milky Way's implied rate of energy loss would drain our galaxy's energy on a much shorter timescale than the galaxy's inferred age. It got worse when in the middle of the 1970 decade, the build of other Weber bar experiments by other groups around the world failed to detect such signs. By the end of the 1970 decade, the consensus was that Weber's detections were some kinds of noise.

The first indirect evidence of gravitational waves was discovered in 1974 by Russell Alan Hulse and Joseph Hooton Taylor Jr., using their discovery of the first binary pulsar. Results were published in 1979, showing the measure of the orbital period decay of the, so-called, Hulse-Taylor pulsar, which precisely describes the angular momentum and energy loss due to gravitational radiation emission predicted by general relativity. A discovery that gave them the 1993 Physics Nobel Prize.

This indirect detection of gravitational waves motivated further searches, despite Weber's discredited result. Some groups continued to improve on Weber's original concept. Using very low temperatures (cryogenic) for the bars, in high-vacuum systems and under vibrational isolation. There were many of these projects around the World. One of these groups built a Niobium bar resonant-mass gravitational wave detector [10]. In this detector, the vibrations caused by the passage of gravitational waves in the niobium bar are measured by a microwave parametric transducer. In this system, microwaves are pumped into a microwave cavity and the vibrations of the microwave cavity are connected to the niobium bar causing microwave signals in the microwaves to leave the cavity. This signal now must be amplified, but it mixes with the original microwave signal, which is too strong for the low-noise microwave amplifier; then the microwave carrier signal is removed by the use of an interferometer that cancels only the microwave carrier. A similar system can be seen in **Figure 1**. This is another use for interferometers in gravitational wave detectors; unfortunately, this kind of detector never made a detection, maybe because of a poor choice in the frequency range [11].

Other experimental groups pursued gravitational wave detection using laser interferometers. This idea of using appears to have been around for a long time by several independent groups, for example in 1962 ME Gertsenshtein and VI Pustovoit [12] and in 1966 by the group of Vladimir B. Braginskii. The first prototype appeared in the 1970 decade built by Robert L. Forward and Rainer Weiss. In the following decades, increasingly sensitive detectors were constructed, culminating in LIGO and Virgo detectors.

After years and years of null results, the first detection of gravitational waves was made by LIGO on September 14, 2015, as the signal, named GW150914, probably came from the merger of two black holes [13, 14]. A year earlier, LIGO could have been brought down when scientists from the BICEP2 (Background Imaging of Cosmic Extragalactic Polarization 2) experiment claimed to have detected a weak signal in the CMB (Cosmic Microwave Background) that appeared like evidence of gravitational waves originating in the beginning universe. This evidence, according to researchers, could have been a smoking gun proof of the theory of cosmic inflation, which

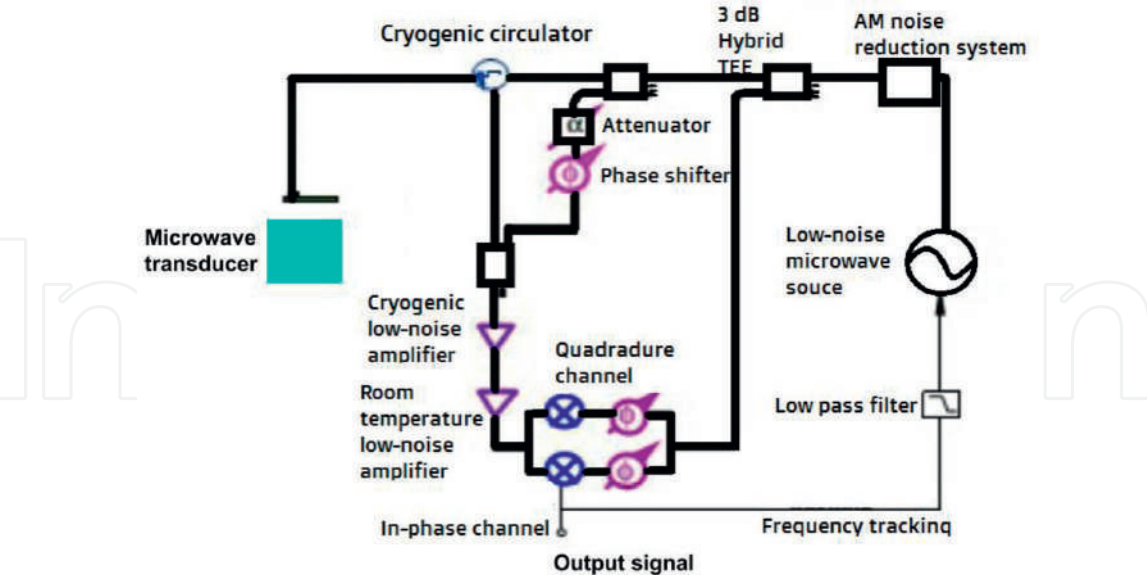


Figure 1. Schematics of a similar electronics of Niobe gravitational wave detector showing a microwave interferometer (between the cryogenic circulator and the cryogenic low-noise amplifier) used to cancel the microwave carrier signal that will degrade the performance of the cryogenic low-noise amplifier.

postulates that very shortly after the Big Bang (10^{-32} seconds after), the expanding universe experienced a period of very rapid expansion (a factor of 10^{26} times). This fast expansion would have created ripples over the CMB, the fossil cosmic radiation that fills the universe being the first detectable electromagnetic radiation in Universe history. However, the BICEP2 signal detected could be explained also by Milky Way dust, making the scientists withdraw the claim that gravitational waves had been detected.

3. Detection

The interferometry system essentially works by measuring the variations that occur in light beams, which are arranged along two different arms. This analysis occurs when we observe the variations and interferences in the return of the light beams, which overlap, since according to the Theory of Relativity light always travels the same distance using the same time, this is our ideal ruler, eliminating the error of a form of measurement that also suffers from the geometric variations caused by ripples. All this technology must be sensitive enough to be able to detect variations of less than a thousandth of a proton.

A powerful laser beam passes through the beam splitter allowing the two generated beams to have the same phase and to be separated perpendicularly by the arms of 4 km each; at the end, they are reflected by the mirrors [13]. Everything was designed so that normally the phases of the waves of the originally emitted light beam and the reflected one generate a destructive effect, so nothing is detected by the photodetector. For the occasion of a gravitational wave passing by the Earth, causing spacetime expand and contract infinitesimally in one direction, thus generating interference arising from the physical property of the wave behavior of light when the phases produce a more constructive effect, thus a signal is detected. **Figure 2** shows the schematics of such a detector.

This is not so straightforward, as the gravitational wave passes through the detector, the gravitational wave also changes the spacetime between the two mirrors, if this

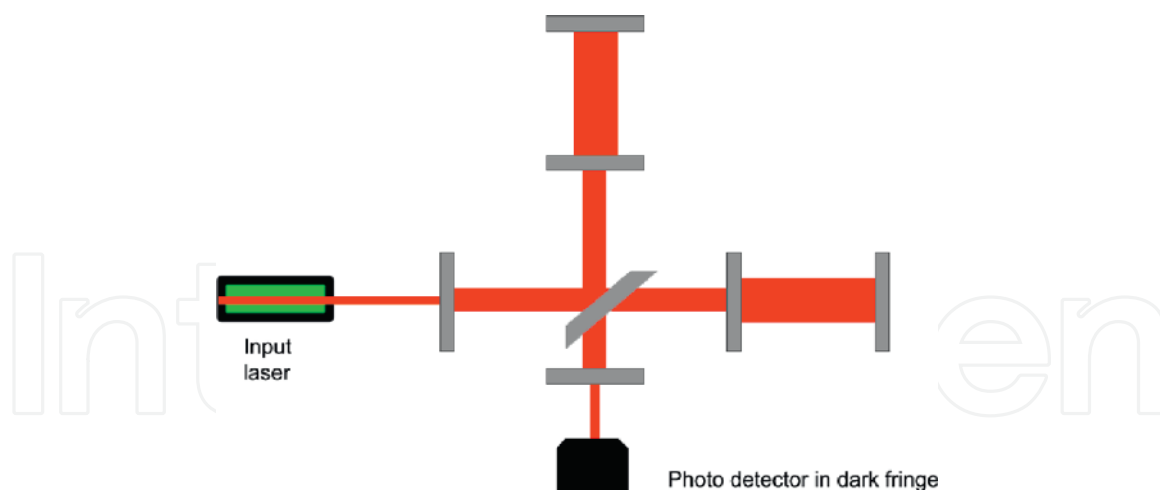


Figure 2.
 Schematics of a laser-interferometric GW detector.

space was made of some material, the length of this material will also change by the gravitational wave, but the passage of gravitational wave does not change the speed of light, then the laser will travel in a shorter time in one arm and a larger time in the other arm then changing the interference pattern in the photodetector.

The fact that there are two observatories is a way of circumventing the possibility of confusing the detection of small earthquakes or some other local source of noise since when detecting a signal, this signal will be compared with that detected by the other observatory. It is only confirmed that this jolt was generated by gravitational waves if the generated signal has the same characteristics, for example, exactly the same profile in frequencies, since the observatories are exactly the same. Importantly, this all takes place in a vacuum, thus ensuring that the light will not have an unstable medium that could alter it in some way. Among the improvements to the observatories, the laser was updated to generate a higher frequency, there was an implementation of fused silica in the mirrors to reduce random mirror movements, and also their suspension was improved to reduce thermal noise and seismic isolation, making the observatories more sensitive for detection [14].

3.1 Indirect

In 1974, the most plausible indirect detection of gravitational waves was made by Joseph Taylor, Jr. and Russell Alan Hulse, when observing pulsars surrounding a neutron star (neutron stars are less dense cousins of black holes). That is the Hulse-Taylor binary, a pair of stars, which is a pulsar [15]. The characteristics of its orbit can be deduced from the Doppler shift of radio signals emitted by the pulsar. Each of the stars is about 1.4 M (M being the mass of the Sun) and the radius of their orbits is around 0.013 of the distance between Earth and Sun, smaller than the diameter of the Sun. The combination of smaller separation and bigger masses means that the energy emitted by the Hulse and Taylor binary will be much larger than the energy emitted by the Earth and Sun system by a factor of approximately 10^{22} times.

Information about the orbit can be used to estimate the amount of energy and angular momentum that would be emitted in the form of gravitational radiation. As the energy is emitted, the pulsars must get closer to each other. Measurements in the Hulse-Taylor system were performed over 30 years ago. The change in the orbital

period corresponds to the prediction of gravitational radiation, assumed by general relativity to be within 1 part in 500. Russell Hulse and Joe Taylor, in 1993, were awarded the Physics Nobel Prize for this remarkable work, which was the first indirect evidence of gravitational radiation. This binary system, from the present until the time of the merger, is estimated to have a lifespan of a few hundred million years [16].

3.2 Direct

After that scientists were motivated to prove its existence. In the mid-1990s they were simulating the Black Hole merger, until the arrival of the Laser Interferometer Gravitational-Wave Observatory (LIGO) and the Italian Gravitational Wave Interferometer Detector (Virgo) at the end of the 20th century made slow progress needing much improvement. The challenge was not the physics itself or the equipment only, but the math behind it. Einstein's equations are called constraint equations, in which the solutions must always satisfy specific conditions, which is difficult since there are 10 equations with thousands of terms [17]. These simulations were necessary as the detectors needed a set of templates for the detected signal in order to establish the source of the signal, but using numerical relativity the set of these templates is still being built. Just to remember that Bayesian statistics is used in the detection.

In late 2015, researchers from the LIGO (Laser Interferometer Gravitational-Wave Observatory) project observed "distortions in spacetime" caused by a pair of black holes, about 30 solar masses each, in the process of merging [14, 17]. The signal was detected in the two LIGO sites on September 14, 2015 at 6:50:45 a.m. PDT, the event was named GW150914. The signal oscillated from 35 Hz to 250 Hz, with a time difference of 7×10^{-3} s between the detection of each observatory, and a maximum amplitude of 1.0×10^{-21} . Thus, coinciding with the shape predicted by Einstein almost exactly 100 years ago for an encounter of massive bodies, in the case of black holes that surround each other until they meet and merge, thus resulting in a significant warping in spacetime. To the relief of many, the merger took place at a distance of ~1.3 billion light-years from Earth. The masses of the initial black holes were 29 M and 36 M, (solar mass, M, approximately 1.99×10^{30} kg); the mass of the resulting black hole was 62M, and approximately 3.0 Mc^2 of energy was converted into gravitational waves to the rest of the Cosmos [14]. The signal of this measurement can be seen in Ref. [14]: the detected signal measured in the two observatories (located in Hanford, WA e Livingston, LA) are shown. First row shows the signal detected in the interferometers; it is shown a difference in time signal over the signal at the Louisiana observatory due to difference in the signal arrival time. Second row shows the expected signal of signal for the optimal source template previously calculated. Third row shows the residuals from rows 1 and 2. Row 4 shows the signal in the frequency domain against time.

In June 2016, the second burst of gravitational waves from merging black holes was announced, suggesting that such detections will soon become routine and part of a new kind of astronomy [18].

On June 1, 2017, for the third time, scientists announced that they had detected the infinitesimal reverberations of spacetime [19].

4. The real detectors

The interferometric gravitational wave detectors are very complex machines, besides being very big vacuum systems, need to have very powerful lasers, and so on.

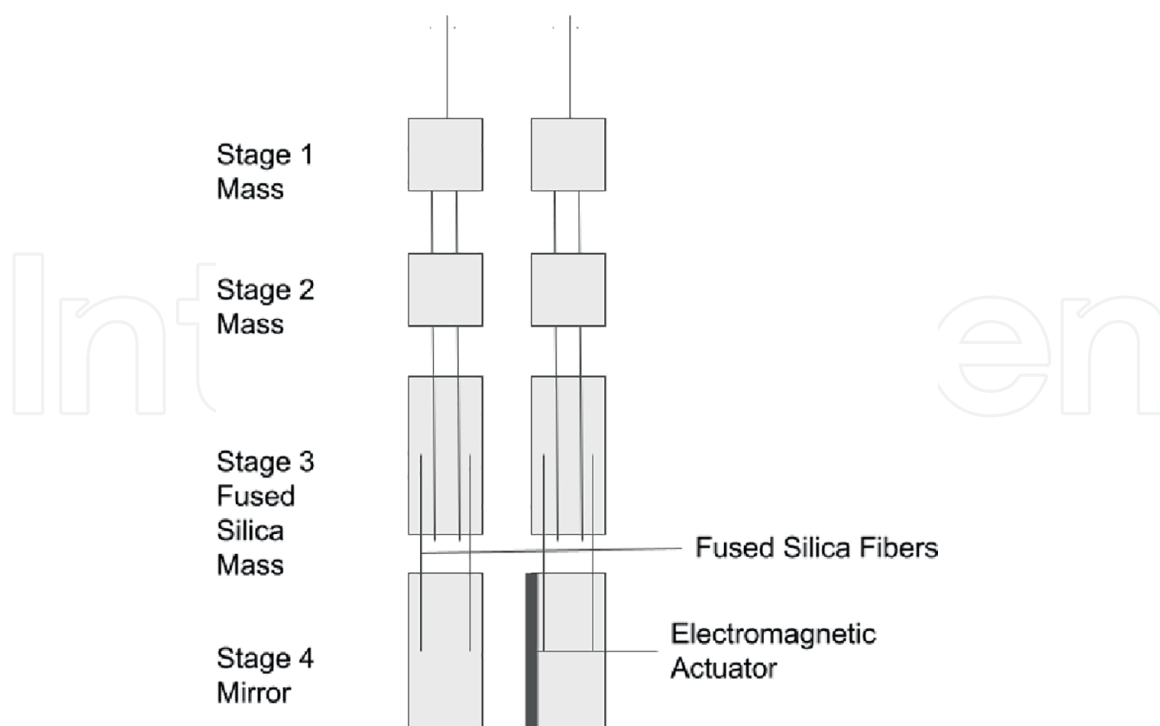


Figure 3.
 Schematics side view of the mirror suspension system of the LIGO detector showing the electrostatic actuator which is used to keep the detector locked in.

The interferometer must be set in a dark fringe condition, but the mirrors are connected to the ground by the suspension, so they vibrate what could change the dark fringe condition. Then a very good suspension that attenuates the vibrations is used, **Figure 3** shows an example of such suspension (this example is about the LIGO detector). The Italian detector Virgo has a more sophisticated suspension which makes this detector more sensitive at lower frequencies.

The Virgo suspension is more complex, it is composed of an inverted pendulum and 6 masses suspended by its center, plus a collection of 18 LVDTs (Linear Variable Displacement Transducers), 5 accelerometers, 23 coils, three piezoelectric devices and 21 motor drivers. All these devices together are called the super attenuator. With a super attenuator for every suspended mirror.

These details show that it is very difficult to keep the interferometer locked in, it also depends on active systems.

But how sensitive the interferometer must be to make such measurements. The first measurement of gravitational waves was of displacement 10^{-18} , as the arms are 4 km long, and the variation in length was 4×10^{-15} . As the power inside the arms is 100 kW with an input power of 20 W, has a recycling factor of 5000 which makes the real sensitivity of the interferometer close to 10^{-12} m.

5. Conclusion

The Gravitational wave interferometric detector successfully detected gravitational waves with unprecedented sensibilities, for the position of the mirror the measurement precision was done in an order of 10^{-18} meters over square root of Hz. For such achievement, the mirror position should be stable for a factor of 10^{-13} m r.m.s.

Acknowledgements

The author acknowledges Conselho de Pesquisa e Desenvolvimento Científico (CNPq, Brazil) for Grant #312454/2021-0 and Fundação de Amparo à Pesquisa do Estado de São Paulo (FAPESP) Grant #2013/26258-4.

Conflict of interest


The authors declare no conflict of interest.

Author details

Carlos Frajuca
Rio Grande Federal University, Rio Grande, RS, Brazil

*Address all correspondence to: frajuca@gmail.com

IntechOpen

© 2022 The Author(s). Licensee IntechOpen. This chapter is distributed under the terms of the Creative Commons Attribution License (<http://creativecommons.org/licenses/by/3.0>), which permits unrestricted use, distribution, and reproduction in any medium, provided the original work is properly cited. 

References

- [1] Einstein A. Näherungsweise Integration der Feldgleichungen der Gravitation. Sitzungsberichte der Königlich Preussischen Akademie der Wissenschaften Berlin. 1916; **part 1**:688-696
- [2] Einstein A. Über Gravitationswellen. Sitzungsberichte der Königlich Preussischen Akademie der Wissenschaften Berlin. 1918; **part 1**:154-167
- [3] Dave F. Einstein's gravity theory passes toughest test yet: Bizarre binary star system pushes study of relativity to new limits. Phys.Org. Internet. 2013. Available from: <https://phys.org/news/2013-04-einstein-gravity-theory-toughest-bizarre.html>
- [4] What is a gravitational wave?: NASA Space Place. spaceplace.nasa.gov. Internet. 2017. Available from: <https://spaceplace.nasa.gov/gravitational-waves/en/>
- [5] Collins H. Gravity's Shadow: The Search for Gravitational Waves. Chicago: University of Chicago Press; 2004
- [6] Rainer Weiss, Barry Barish and Kip Thorne win 2017 Nobel Prize for Physics (in English). physicsworld.com. Internet. 2017. Available from: <https://physicsworld.com/a/2017-nobel-prize-for-physics-winners/>
- [7] Heaviside O. A gravitational and electromagnetic analogy. The Electrician. 1893;**31**(18):5125-5134
- [8] Stanley AE. The propagation of gravitational waves. Process Royal Society. 1922;**102**:268-282
- [9] Levin J. Black Hole Blues and Other Songs from Outer Space. The Bodley Head Publishing House; 2016
- [10] Tobar M, Locke CR, Ivanov EN, Heng IS, Blair DG. Accurate calibration technique for a resonant-mass gravitational detector. The Review of Scientific Instruments. 2000;**71**:4282-4285
- [11] Frajuca C, Prado ARC, Souza MA. The challenge of calibrating a laser-interferometric gravitational wave detector. Astronomische Nachrichten. 2021;**342**:115-122
- [12] Gertsenshtein ME, Pustovoit VI. On the detection of low frequency gravitational waves. Soviet Physics JETP. 1963;**16**(2):433-435
- [13] LIGO's interferometer. 2022. Available from: <https://www.ligo.caltech.edu/page/ligos-ifo>
- [14] Abbott BP et al. Observation of gravitational waves from a binary black hole merger. Physical Review Letters. 2016;**116**(6):061102
- [15] Weisberg JM, Taylor JH. Relativistic binary pulsar B1913+ 16: Thirty years of observations and analysis. 2004; arXiv:astro-ph/0407149
- [16] Damour T. The discovery of the first binary pulsar. Classical and Quantum Gravity. 1974, 2015;**32**(12):124009
- [17] Castelveccchi D, Witze W. Einstein's gravitational waves found at last. Nature News. 2016:19361
- [18] Focus: LIGO Bags another Black Hole Merger. Journal "Physics". 2016;**9**:68

[19] LIGO snags another set of gravitational waves Spacetime vibrations arrive from black hole collision 3 billion light-years away by Emily Conover Internet. 2017. Available from: <https://www.sciencenews.org/article/ligo-snags-another-set-gravitational-waves>. [Accessed: February 15, 2022]